Constraining mountain front tectonic activity in extensional setting from geomorphology and Quaternary stratigraphy: A case study from the Matese ridge, southern Apennines

Ettore Valente [a], Jamie T. Buscher [b, c], Fred Jourdan [d], Paola Petrosino [a], Steven M. Reddy [d], Stefano Tavani [a], Amerigo Corradetti [e], Alessandra Ascione [a, *]

[a] Department of Earth, Environment and Resources Sciences - DiSTAR, University of Naples Federico II, Complesso Universitario Monte Sant'Angelo, 80126, Naples, Italy
[b] Andean Geothermal Center of Excellence (CEGA), Universidad de Chile, Plaza Ercilla 803, Santiago, Chile
[c] Department of Geology, Facultad de Ciencias Físicas y Matemáticas, Universidad de Chile, Plaza Ercilla 803, Santiago, Chile
[d] School of Earth and Planetary Sciences, Curtin University, GPO Box U1987, Perth, WA6845, Australia
[e] Department of Petroleum Engineering, Texas A&M University at Qatar, Education City, Doha, Qatar

ARTICLE INFO

Article history:
Received 3 April 2019
Received in revised form
14 June 2019
Accepted 1 July 2019
Available online 15 July 2019

Keywords:
Morphotectonics
Active tectonics
Quaternary
Southern Apennines
Italy

ABSTRACT

Rugged peaks, large intermontane basins and frequent seismicity all characterize the active extensional tectonic setting of the southern Apennines. The Matese ridge typifies the active tectonic setting of the southern Apennines with steep carbonate mountain fronts and large depositional centres. Moderate to high magnitude earthquakes have affected the northern, western and eastern sectors of the Matese ridge in historical times. However, the seismogenic potential of the extensional fault system bounding the southern Matese mountain front has not been fully assessed to date. To unravel the active tectonic setting of the southern Matese mountain front, we have carried out a comprehensive geomorphological and tectonic-geomorphology investigation of the mountain front and its piedmont and have constrained results through chronological (i.e., tephrostratigraphical and $^{40}Ar/^{39}Ar$) and structural data.

Our study highlights that in the last ~600 ka, activity along E-W trending normal faults has identified a locus of higher slip rate tectonic activity in the central part of the analysed mountain front. These active E-W-striking normal faults are inherited, reactivated structures, which have interacted with newly formed NW-SE-striking normal faults during NE-SW extension active on the regional scale, causing fault bending and local extension to be oriented N-S. Consequently, lower slip rates have been recorded along the NW-SE-striking normal faults at the north-western and south-eastern tips of the southern Matese front. The long-term displacement rate of the fault system at the boundary of the central part of the southern Matese front is consistent with mean values of displacement of faults that, in the southern Apennines, show evidence of activity during the late Quaternary. Despite strong historical seismicity clustering primarily around the study area, our data highlight that it cannot be ruled out that moderate to high magnitude seismicity could affect the southern Matese mountain front.

Our case study represents an example of the possible modes of formation and evolution of mountain front-basin systems in extensional setting, and shows how the combination of different data sets allows unravelling the interaction between tectonic, erosional and sedimentary processes, which lead to landscape evolution of active mountain belts.

1. Introduction

The geomorphological analysis of mountain fronts and related piedmont in actively extending areas provides fundamental clues to the reconstruction of tectonic activity of range-bounding faults on both short- and long-time scales (Bull, 2007). Mountain front

* Corresponding author.
E-mail address: alessandra.ascione@unina.it (A. Ascione).

escarpments created by sustained uplift along active extensional faults may persist far after tectonic activity has ceased. However, geomorphic features of mountain fronts may provide clues about both the state and rates of activity of range-bounding structures (e.g., Wallace, 1977; Hovius, 1996; de Polo and Anderson, 2000; Miccadei et al., 2004; Frankel and Pazzaglia, 2006; Bull, 2007, and references therein). The concentration of different erosional processes at mountain fronts makes deciphering the influence of tectonic activity on landscape development difficult. For example, inferences of tectonic and recent fault activity along mountain fronts may be affected by lithologic controls on fault-escarpment morphologies, such as escarpments formed in hard rock maintaining a much steeper profile and straighter plan form than those formed in soft rock (Young, 1972). The rate of deposition in piedmont areas may also be critical, with strong allogenic sedimentary inputs from, for example, volcanic/pyroclastic material, eventually outpacing the tectonic activity rate. This would result in the masking of new scarp offsets, thus substantially removing near-fault evidence of slip (e.g., Ascione et al., 2007). Furthermore, local base level rise triggered by abundant sedimentary inputs in the hanging wall basin, or relative sea-level rise, can mask continuing topographic growth of the range on a larger scale (e.g., Viseras et al., 2003). In the absence of such factors, the erosion and deposition dynamics at mountain fronts, although modulated by climatic processes, respond primarily to the fault-slip induced creation of accommodation space.

In extension-dominated regions, significant information on the overall balance between denudation of the uplifting footwall and deposition in the downthrown hanging wall can be obtained from the geomorphic features of mountain fronts (e.g., Ellis et al., 1999). Qualitative parameters and quantitative indices describing the mountain front − piedmont system, and in particular the profile and plan form of mountain fronts, the morphology of alluvial fans and drainage basins, and the longitudinal profile of streams (Burbank and Anderson, 2001; Kirby and Whipple, 2001; Keller and Pinter, 2002; Viseras et al., 2003; Harkins et al., 2005; Regalla et al., 2007; Bull, 2007; Whittaker et al., 2008; Amato et al., 2018), may reveal information essential to the assessment of the state and/or rate of activity of mountain escarpment faults.

The state and style of activity and tectonic framework of the extensional fault system that bounds the southern mountain front of the ~2000 m high Matese carbonate ridge have been investigated in this work. The Matese ridge is located in the axial belt of the southern Apennines mountain chain. The Apennine axial belt is currently undergoing NE-SW-oriented extension, roughly orthogonal to the main trend of the mountain belt (e.g., D'Agostino, 2014). Consistent with NE-SW extension are focal mechanisms of strong ($M > 6$) earthquakes that have affected the Apennine chain over the last few decades. Several strong earthquakes ($Mw \sim 7$) associated with seismogenic zones located west and north of the Matese ridge have occurred in the last few centuries (e.g., Serva et al., 2007; DISS Working Group, 2018; Rovida et al., 2016). The seismogenic potential of NW-SE trending fault systems in the western part and northern boundary of the Matese ridge has been recently assessed based on geological/geomorphological datasets (Boncio et al., 2016; Amato et al., 2017; Galli et al., 2017; Ferrarini et al., 2017). However, only rare and sparse historical earthquakes, with low to moderate macroseismic intensities, have affected the region that includes the southern part of the Matese ridge and the adjacent alluvial basin (Valente et al., 2018), with no seismogenic source, or sources, identified to date (e.g., DISS Working Group, 2018).

With the aim of unravelling the late Quaternary tectonic framework of the Matese area, we have carried out a detailed study of the southern Matese mountain front and its piedmont area using a comprehensive geomorphological approach that combines morphometrical and morpho-stratigraphical data, which has been integrated with analysis of structural geology data. In order to construct a chronological framework for the Quaternary tectonics setting, we have applied geochronological ($^{40}Ar/^{39}Ar$) and tephrostratigraphical analyses to Quaternary deposits, which crop out both in the Matese Ridge piedmont and in adjacent alluvial basins.

2. Geological setting and historical seismicity of the study area

The Matese Ridge is located in the northern part of the southern Apennine fold-and-thrust belt. The southern Apennine mountain belt was accreted in the Miocene to early Pleistocene, coeval with back-arc extension and the opening of the Tyrrhenian Sea (e.g. Butler et al., 2004, and references therein). Since the early Pleistocene, active extension in the southern Tyrrhenian basin has created deep grabens along the southwestern margin of the southern Apennines (e.g. Sartori, 1990; Savelli and Schreider, 1991). In some of these coastal grabens, intense eruptive activity has occurred leading to the formation of large volcanic edifices, including the Roccamonfina Volcano and Phlegraean Fields (Fig. 1). Crustal shortening in the southern Apennines ceased in the Middle Pleistocene (Patacca and Scandone, 2001), when NE-SW-oriented horizontal extension became dominant in the mountain belt (e.g., Cinque et al., 1993; Hyppolite et al., 1994; Montone et al., 1999). Extensional faults that dissect the thrust belt (Butler et al., 2004) are also responsible for the active tectonics and seismogenesis in the southern Apennines (e.g., Cello et al., 1982, 2003; Ascione et al., 2007, 2013).

The Apennine accretionary wedge is composed of tectonic units that consist of Mesozoic-Tertiary carbonate platform/slope successions (Apennine Platform) and pelagic basin successions (e.g., Molise basin), stratigraphically overlain by Neogene foredeep and wedge-top basin sediments (Ascione et al., 2012: Vitale and Ciarcia, 2013; Fig. 1). The Apennine accretionary wedge is tectonically superimposed onto the buried Apulian Platform, which consists of a Mesozoic-Tertiary shallow-water carbonate succession that outcrops locally in the southern sectors of the chain (Mazzoli et al., 2008, 2014) and throughout the foreland to the NE (Shiner et al., 2004 and references therein).

The Matese ridge consists of mainly Mesozoic carbonate rocks of the Apennine Platform, which are locally covered by Miocene wedge-top deposits (Fig. 1). The Mesozoic carbonates are composed of Triassic dolostones and Jurassic to Cretaceous inner-platform carbonates extending northward to by-pass and slope facies successions. Differentiation between these depositional environments started during an early Jurassic rifting event, as revealed by the occurrence of Lower Jurassic extensional faults (e.g. Iannace et al., 2005). These faults are mostly E-W striking and were reactivated during Miocene shortening with minor reverse displacement (Calabrò et al., 2003). Carbonates of the Matese ridge are thrusted northward over Mesozoic - Tertiary Molise Basin successions. These units are superimposed onto the buried carbonates of the deformed Apulian Platform (Butler et al., 2000 and references therein; Calabrò et al., 2003, Fig. 1).

The Matese ridge is dissected by NW-SE and E-W trending high-angle faults activated with the Quaternary extensional regime (Butler et al., 2004 and references therein). Major extensional fault zones bound the Matese ridge on the SW and NE (namely, the South Matese Fault System and North Matese Fault System, respectively; Fig. 1) and dissect middle part of the ridge. Late Quaternary activity of all of these structures has been recently assessed (Boncio et al., 2016; Ferranti et al., 2015; Galli et al., 2017; Ascione et al., 2018). Fault activity has caused the formation of two large intermountain basins, the Alife and Bojano basins, which bound the Matese ridge

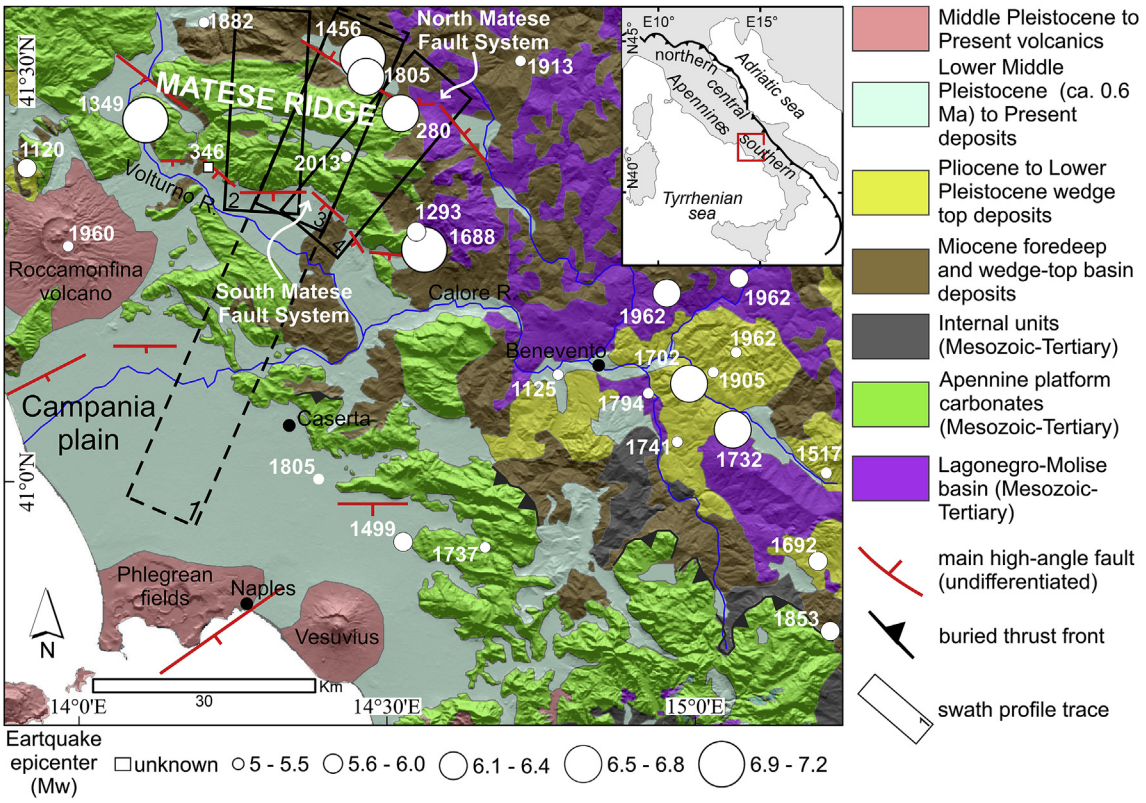

Fig. 1. Geological map of the Southern Apennines (modified from Ascione et al., 2013). The Matese ridge is located in the northern sector of the map. White circles indicate historical earthquakes, with location and magnitude determined by Rovida et al. (2016) except for the 280 BC, 346, 1349, 1456 and 1805 earthquakes, which had locations derived by Galli and Naso (2009). Dashed and continuous line boxes indicate location of swath profiles shown in Fig. 2.

to the SW and NE, respectively (Corniello and Russo, 1990; Aucelli et al., 2013; Amato et al., 2014; Ascione et al., 2018). The southern boundary of the Matese ridge is identified as an E-W-oriented gravimetric lineament (Luiso et al., 2018). Based on geophysical data, the depth of the top of the carbonates in the Alife basin is located below the sea level (Corniello and Russo, 1990), in stark contrast to the ~1300 m height of the carbonates at the boundary of the Matese mountain front. Logs of shallow wells indicate that the Alife basin is filled with a several hundred meters thick succession of alluvial fan gravels, which extends laterally and downward to fine-grained sediments locally interlayered with pyroclastic deposits and travertine and calcareous tufa beds (Corniello and Russo, 1990). Ascione et al. (2018) have correlated the fine-grained sediments recovered in the subsurface of the Alife basin to terraced sediments with comparable features (labelled Ailano lacustrine succession) cropping out in the NW part of the basin. Based on relative chronology criteria, lacustrine deposits outcropping in the Ailano area, as well as terraced fluvial and lacustrine deposits that crop out more to the N in the Ciorlano basin (Fig. 3), have been ascribed to the Middle Pleistocene (Ascione et al., 2018).

Most of the Quaternary alluvial deposits in the Matese ridge region are interlayered with pyroclastic deposits. These deposits include distal pyroclastic density currents of the Campanian Ignimbrite (40 ka - Giaccio et al., 2017), the huge caldera-forming Phlegraean Fields eruption, which often outcrop in the valley cuts to the W and S of Matese ridge. In addition, Middle Pleistocene scattered products from explosive activity of Roccamonfina volcano have been identified to the north of the Matese massif (Bojano alluvial basin), mostly as intermediate to distal pyroclastic density current deposits even though poorly preserved pyroclastic fall layers are also sometimes recognized (Amato et al., 2014; Galli et al., 2017).

The Matese ridge is located in the epicentral area of strong historical earthquakes, such as those that occurred in 1349, 1456, 1688 and 1805 (e.g., Esposito et al., 1987; Gasperini et al., 1999; Michetti et al., 2000; Galli and Galadini, 2003; Galadini and Galli, 2004; Di Bucci et al., 2005; Fracassi and Valensise, 2007; Porfido et al., 2007; Serva et al., 2007; Galli and Naso, 2009; Locati et al., 2011; Rovida et al., 2016, Fig. 1). The seismogenic structure responsible for the 1349 earthquake is believed to be a NW-SE trending and SW dipping fault (Galli and Naso, 2009) located to the west of the Matese ridge. The 1688 and 1805 earthquakes have been related to NW-SE-oriented, NE-dipping seismogenic sources located at the north-eastern and northern boundaries of the Matese ridge, respectively (Boschi et al., 1997; Serva et al., 2007; DISS Working Group, 2018). On 29th December 2013, a M_W 5.16 normal-fault earthquake occurred with an epicentre located in the south-eastern part of the Matese ridge (D'Amico et al., 2014; Ferranti et al., 2015; Rovida et al., 2016, Fig. 1). This earthquake, which was characterised by a NE-oriented T-axis (http://cnt.rm.ingv.it/tdmt.html), caused a series of coseismic effects, including landslides and ground ruptures (Valente et al., 2018).

3. Methods

This tectonic geomorphology study of the southern Matese ridge and adjoining alluvial plains has been carried out through a comprehensive analysis of the topography and stream network, combined with stratigraphical analyses of Quaternary deposits, and integrated with new dating and structural geology analyses to discern what areas exhibit differential vertical motion at the surface.

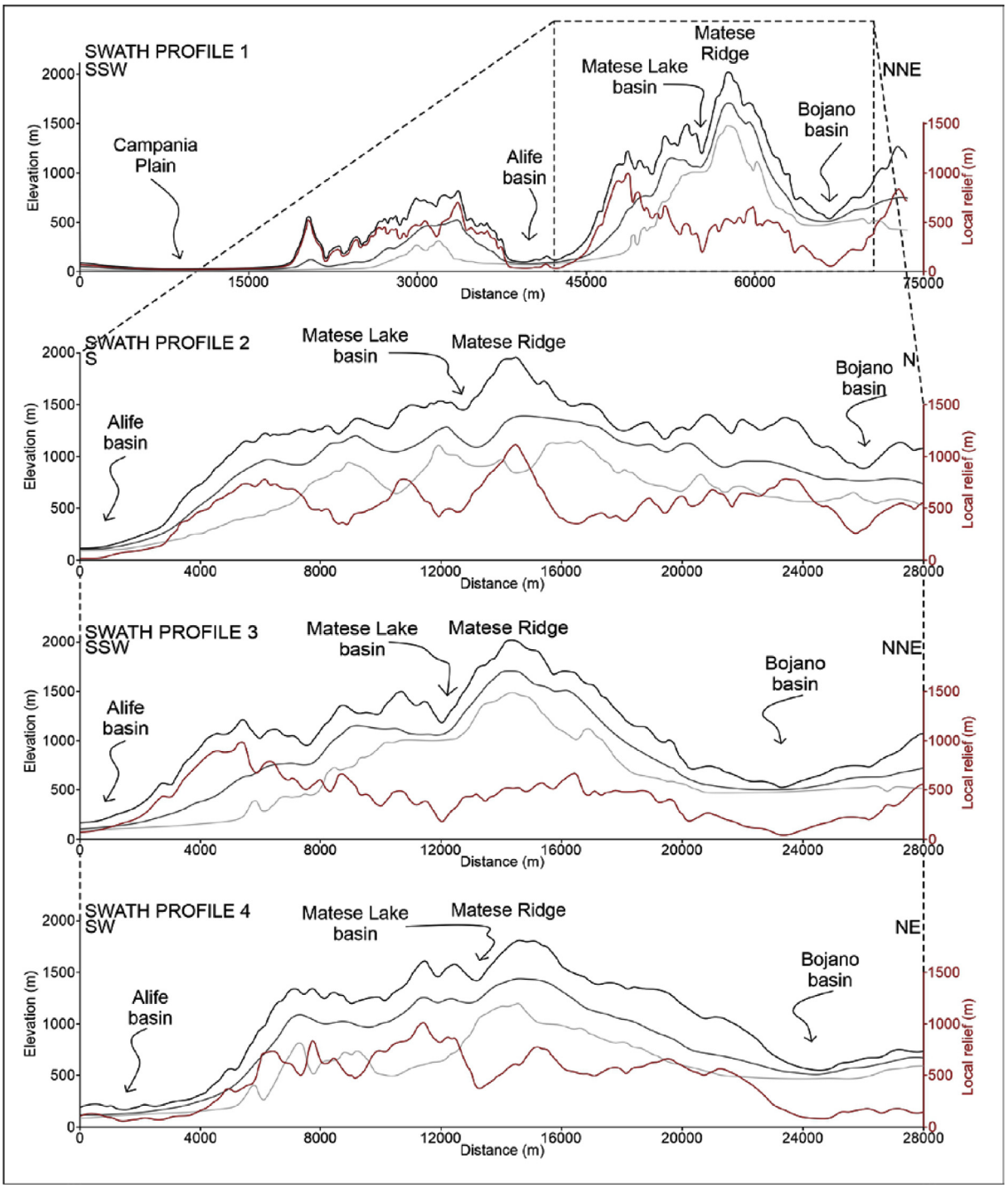

Fig. 2. Swath profiles from the Matese area (see Fig. 1 for locations). Swath 1 is a regional scale profile, with the Matese ridge shown at the end of the profile, whereas swaths 2, 3 and 4 cross the Matese ridge from SW (Alife basin) to NE (Bojano basin). Black line indicates maximum elevation curve, grey line indicates mean elevation curve, light grey line indicates minimum elevation curve and red line indicates relief curve.

The stratigraphical study of Quaternary deposits located at the toe of the Matese mountain front and in the adjoining alluvial basins has included the inspection of published and unpublished logs of shallow boreholes ranging in depth between 20 m and 180 m, aimed at constraining the subsurface depositional environment of the Quaternary deposits. Field surveys have been particularly focused on characterising deposits that both form the piedmont of the Matese mountain front and crop out at the western termination of the ridge, paying more attention to pyroclastic deposits chronologically related to the evolution of the mountain front (Section 3.2).

3.1. *Tectonic geomorphology*

The geomorphological analysis has been carried out using detailed 1:5000-scale digital topographic data from Regione

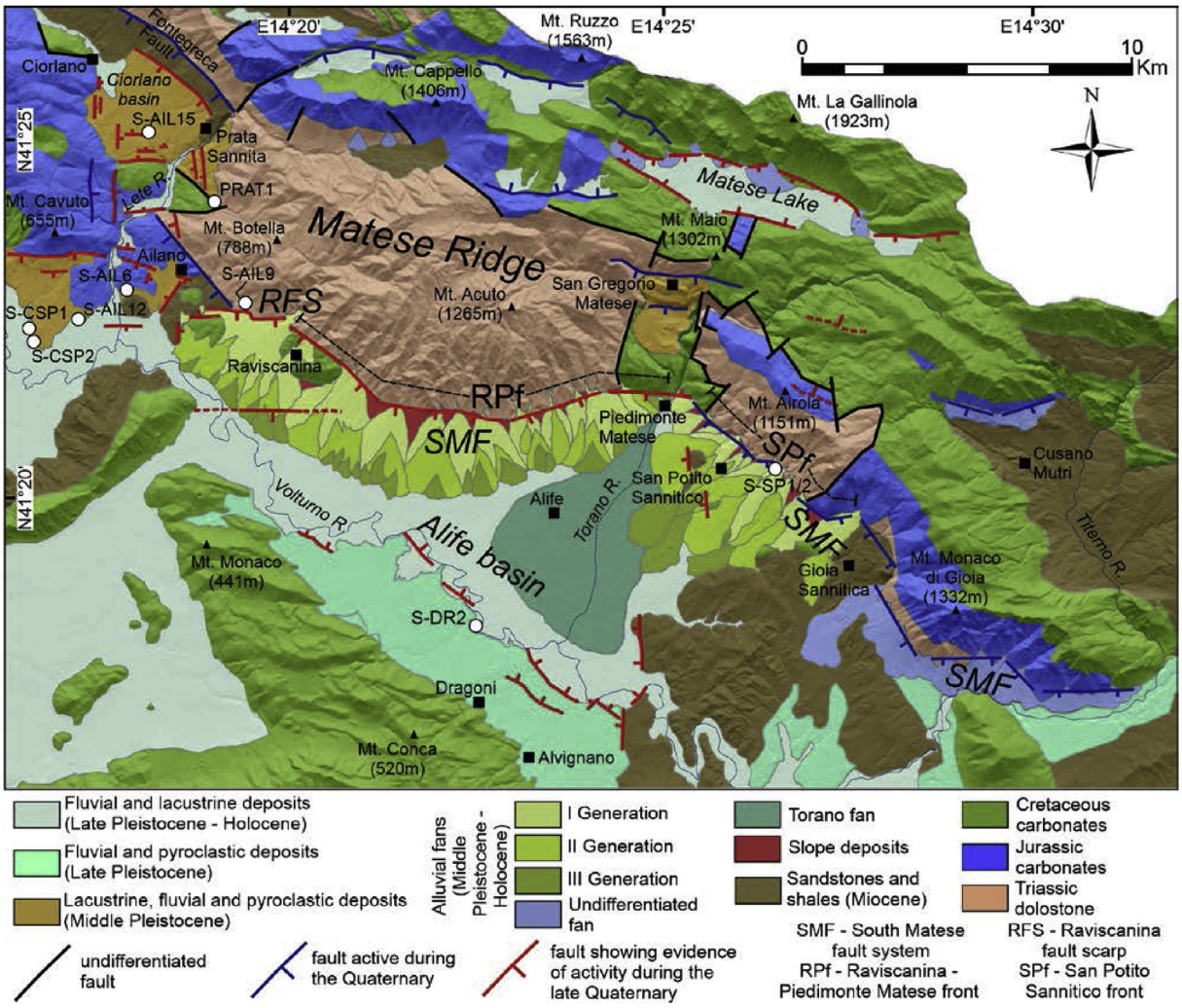

Fig. 3. Geological map of the southern sector of the Matese ridge and the adjoining Alife basin. Undifferentiated faults have been included from the literature (Vitale and Ciarcia, 2018; Sheets 161 – Isernia, 162 – Campobasso, 172 – Caserta and 173 Benevento of the Geological Map of Italy in scale 1:100000, http://www.isprambiente.gov.it/it/cartografia/carte-geologiche-e-geotematiche/carta-geologica-alla-scala-1-a-100000). White dots indicate locations of samples collected for tephrostratigraphical and $^{40}Ar/^{39}Ar$ analysis.

Campania and a high-resolution DTM (10 m horizontal resolution) derived from the topographic data. The topography has been analysed through the construction of swath profiles and the calculation of morphometrical indices (mountain front sinuosity and morphology of drainage basins and alluvial fans) and parameters of the drainage networks.

3.1.1. Swath profile analysis

Swath profiles represent one of the most powerful tools to investigate large-scale features of topography because elevation data is concentrated into a single profile. Maximum, mean and minimum elevation curves derived from swath profile analysis provide useful quantitative information about topographic features within the swath. The elevation parameter is strongly influenced by both rock type and surface uplift, and even if the maximum elevation primarily reflects the relationship between rock resistance and erosion, mean elevation can represent the expression of surface uplift (England and Molnar, 1990). Mean elevation values are in fact modulated by the contribution of minimum elevation, which is often equivalent to the elevation of valley floors, and is a parameter that represents the net result between uplift and fluvial incision.

Swath profiles have been derived from 90 m NASA SRTM Data using the SwathProfiler Add-in of ArcGIS (Pérez-Peña et al., 2017). We adopted the default SwathProfiler Add-in values for both the sampling window (1.5 times the cell size, thus resulting in a 135 m sampling window) and the number of polylines parallel to the swath trace used to derive topographic profiles (resulting in 50 equal-spaced lines). Swath 1 (Fig. 1) is oriented SSW-NNE and is about 75 km long and 10 km wide. Swaths 2, 3 and 4 (Fig. 1) have similar orientations as Swath 1 but are 28 km long and 10 km wide. The swaths cross the Matese ridge, with orientation varying along the ridge so that the swaths could be oriented perpendicular to the main morphostructural features and extend across most of the ridge.

3.1.2. Mountain front sinuosity

Mountain front sinuosity (Bull and McFadden, 1977) is defined by the following equation:

$$S_{mf} = L_{mf} / L_s \quad (1)$$

where L_{mf} is the mountain front length measured at the mountain front – piedmont interface, and L_s is the straight length of the mountain front. S_{mf} values reflect the balance between active

tectonic forces that tend to produce a rectilinear mountain front coinciding with the bounding fault plane and erosional forces that can dissect the mountain front. In tectonically active areas, uplift typically outpaces erosion, leading to rectilinear mountain fronts with low (~1) S_{mf} values, while mountain fronts that are tectonically less active or inactive have higher S_{mf} values due to the dominance of erosion over uplift ultimately leading to river dissection (Bull and McFadden, 1977). S_{mf} values < 1.4 primarily reflect tectonically active mountain fronts whereas S_{mf} values > 3 are typical of tectonically inactive mountain fronts, with the active, erosionally-dominated mountain front being located >1 km from the original active mountain front in some cases (Mahmood and Gloaguen, 2012). In our study, detailed topographic maps (scale 1:5000) have been used to derive values for both L_{mf} and L_s, which have been measured with the ArcGIS 10.3 © ruler tool, and then Smf has been calculated by applying equation (1).

3.1.3. Alluvial fan and drainage basin morphometry

Alluvial fans and related basins have been characterised by geomorphological analysis of detailed topographic maps (scale 1:5000) and 10 m DTMs derived from these topographic maps in a GIS environment, allowing for quantification of morphometrical features representative of the alluvial fan − drainage basin setting. Moreover, we adopted some of the parameters described in Viseras et al. (2003), which include the following: Fan area (Fa, the planimetric area of the fan in km^2); Basin area (Da, the planimetric area of the drainage basin in km^2); Fan slope (Fs, the gradient of the fan measured along the fan axis in degrees); Ratio width-length of the fan (WLF, representative of the elongation of the fan); Ratio width-length of the drainage basin (WLD, representative of the elongation of the drainage basin); Sweep angle (As, the angle between the two outermost channels within each fan in degrees); Incised channel percentage (ICP, the percentage of fan area affected by channel incision). These parameters allow comparisons to be made between alluvial fans developed in different morphotectonic settings and are considered to be sensitive to variations in surface uplift, even in small areas such as mountain fronts (Viseras et al., 2003).

3.1.4. River long profile analysis

River long profile analysis provides useful information about the topographic response to both small- and large-scale tectonic perturbations. In actively uplifting areas, river long profiles may deviate from a theoretical graded profile (Hack, 1957) to exhibit a convex upward shape (Kirby and Whipple, 2001; Attal et al., 2011; Whittaker et al., 2007) that correlates with the timing and spatial distribution of uplift (Whittaker et al., 2007; Whittaker, 2012). In this study, river long profile analysis has been applied to thirty-four rivers dissecting the southern slope of the Matese ridge. Analysed trunks include bedrock-floored rivers extending from the drainage divide to the mountain front toe, excluding areas with alluvial fans. The river network has been analysed with the stream profile tool of Whipple et al. (2007) (http://geomorphtools.geology.isu.edu/Tools/StPro/StPro.htm) in ArcGIS. The convexity index data and knickpoints have been plotted on a hillshade map derived from the 10 m DTM in order to analyse the spatial distribution of these features.

3.2. Geochronological and tephrostratigraphical analyses

In the Matese area, most of the alluvial units (which include alluvial fan, fluvial, alluvial plain and lacustrine facies) have tephra beds that can be used to establish age constraints. Sampling of pyroclastic deposits for geochronological ($^{40}Ar/^{39}Ar$ dating) and tephrostratigraphical analyses was carried out to establish a chronological framework of the units for comparison with the geomorphological-structural data. Besides direct dating of alluvial fan deposits from the Matese mountain front piedmont (which contain only sparse, and in most cases, intensely weathered pyroclastics), the criteria driving the sampling strategy have been the following: (i) constraining the age of alluvial fans by dating pyroclastic deposits covering either the alluvial fan deposits or inset in valleys incised into the alluvial fan deposits; (ii) dating of Quaternary units chronologically related to the Matese mountain front evolution, outcropping near the piedmont belt in the northwest (e.g., lacustrine deposits outcropping in the Ailano and Ciorlano areas; Section 5) and in the southern sector of the Alife basin.

3.2.1. Tephrostratigraphical analysis

The investigated tephra samples were collected primarily from argillified sand to ash-sized deposits, were loose to slightly indurated, and varied in colour from greyish to dark yellow. For the analysis, the samples were first washed thoroughly in deionized water in order to remove the clay fraction and then the remaining material underwent at least three ultrasonic washing treatments lasting 10 min each. The remaining clasts were then dried and sieved with 1 phi sieves. Finally, analysis of the lithological content was carried out for the 1 and 2 phi fractions using a binocular microscope.

After sample preparation and screening, the few well preserved juvenile fragments extracted from the investigated tephras were embedded in epoxy resin and polished for SEM-EDS analysis, which was carried out at DiSTAR at the University of Napoli Federico II. The analytical facility is equipped with an Oxford Instruments Microanalysis Unit, which has an INCA X-act detector and a JEOL JSM-5310 microscope operating with a 15 kV primary beam voltage, a 50−100 mA filament current, a variable spot size, and a 50 s net acquisition time. Measurements were performed with an INCA X-stream pulse processor. Instrument calibration was based on international mineral and glass standards (for full details, see Petrosino et al., 2015). Individual analyses of glass fragments with a total oxide sum lower than 94 wt% were discarded.

3.2.2. $^{40}Ar/^{39}Ar$ dating

From six selected samples from the Matese area, at least 0.5 mg of sanidine crystals measuring 0.1−1 mm were handpicked using a binocular microscope for $^{40}Ar/^{39}Ar$ dating. $^{40}Ar/^{39}Ar$ analyses were conducted at the Western Australian Argon Isotope Facility at Curtin University.

For each of the six samples, fresh sanidine crystals ranging from 215 to 750 μm in diameter were carefully hand-picked using a binocular microscope. The sanidine were thoroughly rinsed with distilled water in an ultrasonic cleaner. Samples were loaded into large wells of one aluminium disc measuring 1.9 cm in diameter and 0.3 cm in depth. These wells were bracketed by small wells that included the GA1550 biotite standard used as a neutron fluence monitor that has an age of 99.738 ± 0.10 Ma (1σ) (Renne et al., 2011). The discs were Cd-shielded to minimize undesirable nuclear interference reactions and irradiated for 20 min at the Oregon State University (OSU) TRIGA reactor in Corvallis, Oregon (USA). The mean J-values computed from the grain standards within the small wells and determined as the average and the standard deviation of J-values of the small wells for each irradiation disc are given along with the raw data in Annex 1. Mass discrimination values range from 0.993078 (±0.04%) to 0.992880 (±0.05%) and were monitored using an automated air pipette and calculated relative to an air ratio of 298.56 ± 0.31 (Lee et al., 2006). Correction factors for interfering isotopes were $(^{39}Ar/^{37}Ar)Ca = 6.95 \times 10^{-4}$ (±1.3%), $(^{36}Ar/^{37}Ar)Ca = 2.65 \times 10^{-4}$ (±0.84%) and $(^{40}Ar/^{39}Ar)K = 7.30 \times 10^{-4}$ (±12.4%) (Renne et al., 2013) for the OSU reactor. The $^{40}Ar/^{39}Ar$ analyses were performed at the Western Australian Argon Isotope Facility at Curtin University using an ARGUS VI multi-collector

noble gas mass spectrometer. For each sample, 14 to 17 crystals were analysed and fused in a single step using a continuous 100 W PhotonMachine© CO2 (IR, 10.4 μm) laser fired on the crystals for 60 s. Each of the standard crystals was fused in a single step. The gas was purified in an extra-low-volume stainless steel extraction line of 240 cm^3 using two SAES AP10 and one GP50 getters and a cryocooler condensation trap. Ar isotopes were measured in static mode using a low volume (600 cm^3) ARGUS VI mass spectrometer from Thermofisher©, set with a permanent resolution of ~200. Measurements were carried out in multi-collection mode using four faraday cups to measure mass 40 to 37 and a low background compact discrete dynode ion counter to measure mass 36. We measured the relative abundance of each mass simultaneously using 10 cycles of peak-hopping and 16 s of integration time for each mass. Detectors were calibrated to each other electronically using air shot beam signals. The raw data were processed using the ArArCALC software (Koppers, 2002) and ages were calculated using decay constants recommended by Renne et al. (2011). All parameters and relative abundance values are provided in individual Annexes (Supplementary Table 1) and have been corrected for blank values, mass discrimination and radioactive decay.

For the determination of a meaningful eruption age, sample ages must include at least three crystals that agree at a 95% confidence level and have a probability of fit (P) of at least 0.05. Ages (Supplementary Table 1) are given at a 2σ level and are calculated using the mean of all plateau steps, weighted by the inverse variances of the individual analytical uncertainties. The final recommended ages given in Section 5.1 are determined by calculating the weighted mean ages of all the plateau steps. Uncertainties include analytical and J-value errors.

3.3. Structural analysis

Structural analysis has been based on detailed field surveys in the area between Ailano and Ciorlano to the west, the Alife basin to the south, and the Matese ridge up to the Matese Lake basin to the north. Field surveys have focused on the tectonic structures affecting the Meso-Cenozoic carbonate bedrock, with ~400 measurements of meso-faults at 30 sites being collected and plotted in stereo-plots for analysis.

4. Geomorphological and morphometrical features of the Matese Ridge mountain front and piedmont

The large-scale topographic features of the study area have been investigated through the construction of a series of swath profiles.

The swath profile 1 (Fig. 2) shows the overall geomorphic setting of the region including Matese Ridge. The profile extends SSW to NNE from the Campania Plain to the Bojano basin. The Matese ridge appears at the end of the swath profile and includes the highest peak in the study area (Mt. Miletto, 2050 m a.s.l.). The presence of high-angle, normal-fault-bounded basins is evident as reflected by the Campania Plain and the Alife and Bojano basins. The Alife and Bojano basins are located to the SW and NE of the Matese ridge, respectively, with the Bojano basin located at a higher elevation than the Alife basin. The southwestern slope of the Matese ridge appears steeper than the north-eastern slope, suggesting that the southwestern slope is younger. Also, the presence of extensional basins within the Matese ridge is evident from the mean and minimum elevation curves, with the largest of which corresponding to the Matese Lake basin. Relief curves tend to increase in the mountain areas and decrease, or even appear relatively flat in the normal-fault-bounded basins. The maximum relief occurs along the southwestern slope of the Matese ridge and progressively decreases towards the NE, with the local minimum corresponding to Matese Lake and Bojano basins.

Swath profiles 2, 3 and 4 (Fig. 2) cross the entire Matese ridge SW to NE from the Alife basin to the Bojano basin and are in the north-western, central and south-eastern parts of the ridge, respectively (Fig. 2). Swath profiles 2 and 3 include the highest peak of the ridge (Mt. Miletto, 2050 m a.s.l.), whereas the highest elevation in swath profile 4 is around 1800 m a.s.l. The three swath profiles show similar features, such as a progressive decrease in relief from SW to NE and a tight grouping of maximum elevation curves between 1200 and 1500 m a.s.l. However, a comparison of the profiles shows that the shape of the southwestern Matese mountain front changes along strike, from convex in the NW (swath profile 2) to part rectilinear/part concave in the centre (swath profile 3) to concave in the SE (swath profile 4; Fig. 2).

4.1. Matese Ridge mountain front and alluvial fan morphology

The Matese Ridge mountain front is formed by a succession of straight fault escarpments with variable orientations. The southeastern part of the mountain front (San Potito Sannitico mountain front, hereinafter SPf; Fig. 3) primarily exhibits a NW-SE orientation, with shorter E-W-oriented segments located in between. The remaining part of the mountain front is highly segmented, consisting of E-W-, NW-SE- and NE-SW-trending straight escarpments that are almost entirely formed in intensely fractured Triassic dolostones (Fig. 3). A continuous alluvial fan belt is present along the entire Raviscanina – Piedimonte Matese sector (hereinafter RPf; Fig. 4) and the SPf. Between the two belts, the Torano river forms a wide, low-slope alluvial fan that gently grades to the Volturno River floodplain (Fig. 3). The bajada that extends along the RPf is bounded on the NW by a straight, E-W-trending scarp that we interpret to be a fault scarp (Raviscanina fault scarp, hereinafter RFS; Fig. 3). The RFS is found in Miocene sandstones in the west and in Triassic dolostones in the east. To the N of the RFS, a raised patch of alluvial fan deposits outcrops at 280 m a.s.l. along the westernmost, NW-SE-oriented segment of the Matese ridge carbonate part of the escarpment (see location of Sample AIL9 in Fig. 3 for reference), while in the hills to the NW of the RFS, eroded lake/alluvial plain and pyroclastic deposits crop out and are described below (Fig. 3; Section 5.2).

The morphometrical features of the RPf and SPf and correlative piedmonts have been analysed and compared. These two sectors differ slightly in terms of sinuosity, with the RPf having a more rectilinear shape (Smf = 1,53) while the SPf is slightly more sinuous (Smf = 1.64).

Three generations of coalesced alluvial fans have been recognized along both the RPf and SPf (Fig. 3). However, the architecture of the alluvial fan bodies from the two mountain front areas is different, with entrenched fans occurring along the SPf, and superimposed fan bodies with apexes poorly indented into the mountain front found along the RPf. Furthermore, while alluvial fans along the RPf form a laterally continuous surface, some outcrops of the Mesozoic-Tertiary substratum (i.e., carbonates and sandstones; Fig. 3) occur among the fans in the piedmont of the SPf. To analyse the morphometrical features of the alluvial fans, the three generations of fans within each drainage basin – alluvial fan system have been grouped together as one fan unit (Fig. 5).

The results of the morphometrical analysis of each alluvial fan – drainage basin system are reported in Table 1 and Fig. 6. Fans located along the RPf (from 1 to 12) are the largest in total area, with an average Fa = 2.51 km^2 and fan 1 having the highest value (Fa = 6.15 km^2) of the two mountain front areas. In contrast, fans located along the SPf (from 13 to 21) are smaller, with an average Fa value of 1.84 km^2 and fan 15 representing the largest fan of the SPf (Fa = 3.13 km^2). A similar pattern is seen for basin area

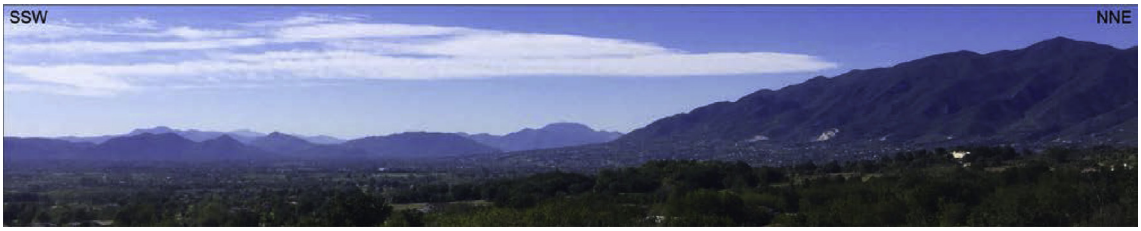

Fig. 4. Panoramic view (from the southeast) of the Raviscanina-Piedimonte Matese sector (RPf) of the southern Matese mountain front, and correlative piedmont graded to the flat-lying Volturno River alluvial plain, visible in the left.

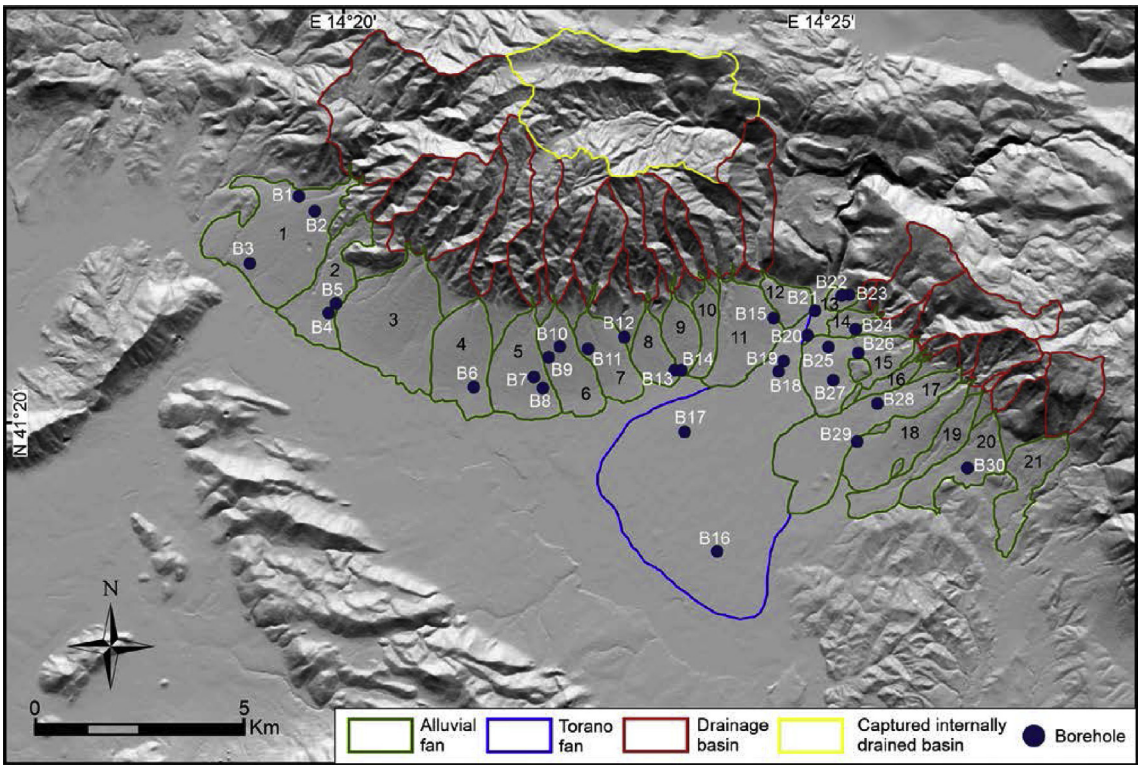

Fig. 5. Map of the alluvial fans (green lines) and drainage basins (red lines) along the southern Matese mountain front. Captured internally drained basin (yellow line) has been excluded from the morphometrical analysis. Borehole locations are also reported. See Supplementary Fig. 1 for borehole stratigraphy. (For interpretation of the references to colour in this figure legend, the reader is referred to the Web version of this article.)

measurements, with higher values found along the RPf (max Ba = 11.29 km^2 for fan 1, mean Ba = 3.11 km^2) compared to the SPf (max Ba = 3.24 km^2 for fan 15, mean Ba = 1.22 km^2). The opposite trend occurs for fan slope, with SPf fans steeper (max slope of 8.48° for fan 13, mean slope of 6.27°) relative to fans located along the RPf (max slope of 6.54° for fan 6, mean slope of 5.57°). The shape of the fans is described by the WLF factor, which shows higher values along the RPf (max = 0.85 for fan 3, mean = 0.57) that decrease along the SPf (max = 0.7 for fan 13, mean = 0.38), thereby indicating that fans are sub-rounded along the RPf and elongated along the SPf. Drainage basins follow a more elongated shape along the RPf (max WLD = 0.63 for fan 1, mean WLD = 0.32) with respect to the SPf (max WLD = 0.68 for fan 13, mean WLD = 0.46). Alluvial fans along the RPf are also characterised by a higher sweep angle (max = 84° for fan 3, mean = 63°) with respect to the SPf (max = 62° for fan 20, mean = 47°), while alluvial fans along the SPf are more incised (max ICP = 16.26% for fan 19, mean ICP = 8.09%) than those along the RPf (max ICP = 9.24% for fan 11, mean ICP = 4.61%).

4.2. Stream profile analysis

The convexity index varies along the southern slope of Matese ridge following an ~E-W trend (Fig. 7). Streams located in the western and eastern extents of the ridge primarily have a concave shape (streams 1, 2, 4, 28, 32, 33 and 34), whereas streams that dissect the RPf are rectilinear to convex (streams 5 to 20), with the highest convexity values found at the core of the RPf (streams 8 to 14). Some of the mapped streams have incised along the eastern and western ends of the domal structure, ultimately reaching the southern divide boundary of the internally drained basins. The shape of the upper reaches varies for these streams based on location, with concave profiles in the west (streams 1, 2 and 4) and convex profiles in the east (streams 21 to 24).

Similar to stream convexity, the knickpoint density also progressively increases towards the RPf (Fig. 7). The relatively low number of knickpoints found at the western and eastern ends of the Matese ridge are thought to be remnant inflection points formed following the capture of small karstic basins (streams 28 to 34). The east-central part of the field area with a moderate number of

Table 1
Morphometrical analysis of the alluvial fans and related drainage basins located along the southern Matese mountain front. Fan and drainage basin locations are shown in Fig. 5.

Fan	Fan area (km^2)	Basin area (km^2)	Fan slope (°)	Ratio width/length of fan	Ratio width/length of the basin	Sweep angle (°)	Incised channel percentage (%)
Raviscanina – Piedimonte Matese front (RPf)							
1	6,15	11,29	5,05	0,81	0,63	73	3,57
2	2,45	1,47	4,97	0,38	0,36	42	8,97
3	5,34	4,07	5,81	0,85	0,53	84	3,55
4	2,77	2,85	5,43	0,57	0,20	65	3,97
5	2,44	2,38	5,63	0,55	0,20	58	2,45
6	1,93	2,87	6,54	0,46	0,24	65	3,62
7	1,74	2,14	6,34	0,56	0,33	76	6,89
8	1,19	1,74	5,54	0,50	0,23	48	7,56
9	1,20	1,47	5,95	0,49	0,21	58	3,33
10	0,98	1,10	5,50	0,27	0,25	52	0,00
11	3,03	2,99	4,92	0,74	0,39	78	9,24
12	0,92	3,00	5,11	0,63	0,22	58	2,17
max	**6,15**	**11,29**	**6,54**	**0,85**	**0,63**	**84**	**9,24**
min	**0,92**	**1,10**	**4,92**	**0,27**	**0,20**	**42**	**0,00**
mean	**2,51**	**3,11**	**5,57**	**0,57**	**0,32**	**63**	**4,61**
San Potito Sannitico front (SPf)							
13	0,32	0,10	8,48	0,70	0,68	50	0,00
14	0,50	2,50	5,59	0,56	0,41	56	5,60
15	3,13	3,24	4,18	0,63	0,47	60	6,10
16	0,52	0,30	6,25	0,19	0,43	36	10,86
17	2,69	0,37	5,58	0,19	0,47	35	4,09
18	2,98	1,35	5,27	0,27	0,52	32	6,71
19	2,04	0,10	6,80	0,16	0,24	50	16,26
20	2,26	0,80	6,05	0,42	0,29	62	11,40
21	2,16	2,23	8,21	0,30	0,62	46	11,81
max	**3,13**	**3,24**	**8,48**	**0,70**	**0,68**	**62**	**16,26**
min	**0,32**	**0,10**	**4,18**	**0,16**	**0,24**	**32**	**0,00**
mean	**1,84**	**1,22**	**6,27**	**0,38**	**0,46**	**47**	**8,09**

knickpoints, some with impressive sharp angular forms found along the disappearing trunk of the Torano River (stream 24) and nearby tributaries, are believed to have formed exclusively by karstic processes based on the random distribution of knickpoint features and dominance of karstic topography throughout the catchment. The highest concentration of knickpoints in the study area is found near or at the domal structure along the RPf. North of the dome, there are a relatively moderate amount of knickpoints believed to represent inflection points of breached drainage divides of former internally drained basins based on the alignment of two knickpoint pairs along the northern part of the dome (Fig. 7). The highest concentration of knickpoints is found along the southern flank of the domal feature, with knickpoints loosely aligned following the curve of the mountain front, and the lack of conspicuous karstic features observed on this flank suggests that these knickpoints may be geomorphic features related to recent surface uplift.

5. Quaternary stratigraphy framework

5.1. Alluvial units from the southern Matese mountain front

Outcrop and borehole data indicate that alluvial fans in the piedmont of the RPf and SPf primarily consist of poorly consolidated carbonate gravels and sands, interbedded with silty – clayey layers and tephra layers. A marked difference in thickness, however, characterises alluvial fans from the RPf and SPf. In Suppl. Fig. 1, we present the stratigraphy of the boreholes with thicknesses >30 m depth from Fig. 5.

Alluvial fan deposits along the RPf have been drilled down to depths >100 m and consist of gravels with local intercalations of sand, silt and clay layers, calcareous tufa and volcanics (boreholes B1 to B15 in Suppl. Fig. 1). Conversely, alluvial fans along the SPf are shallower, with Meso-Cenozoic carbonate bedrock encountered at a few meters to tens of meters depth (boreholes B22 to B30 in Suppl. Fig. 1). The shallow depth of the Meso-Cenozoic bedrock in the SPf piedmont is consistent with the occurrence of bedrock outcrops interspersed between the alluvial fan surfaces (Section 4.1).

With the aim of constraining ages of the alluvial fan deposits, we sampled the following: (1) a 20 cm thick, greyish sandy tephra layer from the upper part of a 1st generation alluvial fan (in the apical portion of the fan, sample S-SP1 in Fig. 8a) from the SPf area, (2) a yellowish, ~70 cm thick, pyroclastic tuff deposit inset in a valley cut into the same alluvial fan deposit of sample S-SP2 (Fig. 8d), and (3) yellowish pyroclastic deposits found within mature, reddish soil, which overlie elevated alluvial fan deposits to the N of Raviscanina (sample S-AIL9, Fig. 8e).

The two younger generation alluvial fans along the RPf and the third-generation alluvial fans from the SPf onlap onto – and thus are essentially coeval with - the Volturno River floodplain. The SPf fans extend onto a wide plateau formed by a distinctive reddish to yellowish ignimbrite deposit more than 8–10 m thick that stands on the southern flank of the Alife basin. Similar ignimbrite deposits, at least >3 m thick, form a dissected plateau inset into the 2nd-order terrace of the Ciorlano basin. A correlation between these ignimbrite deposits and the Campanian Ignimbrite regional stratigraphic marker of Phlegraean origin dated at 40 ka (Giaccio et al., 2017) has been hypothesised by Ascione et al. (2018) based on the facies, thickness and spatial distribution of this deposit. To assess such a correlation, both ignimbrite deposits have been sampled for $^{40}Ar/^{39}Ar$ dating and tephrostratigraphical analyses (Samples S-DR2, Fig. 8b and S-AIL15, Fig. 8c).

5.2. Alluvial units outcropping NW of the Alife basin

The field surveys have allowed better constraints to be made for the stratigraphy of the alluvial deposits outcropping NW of the Alife

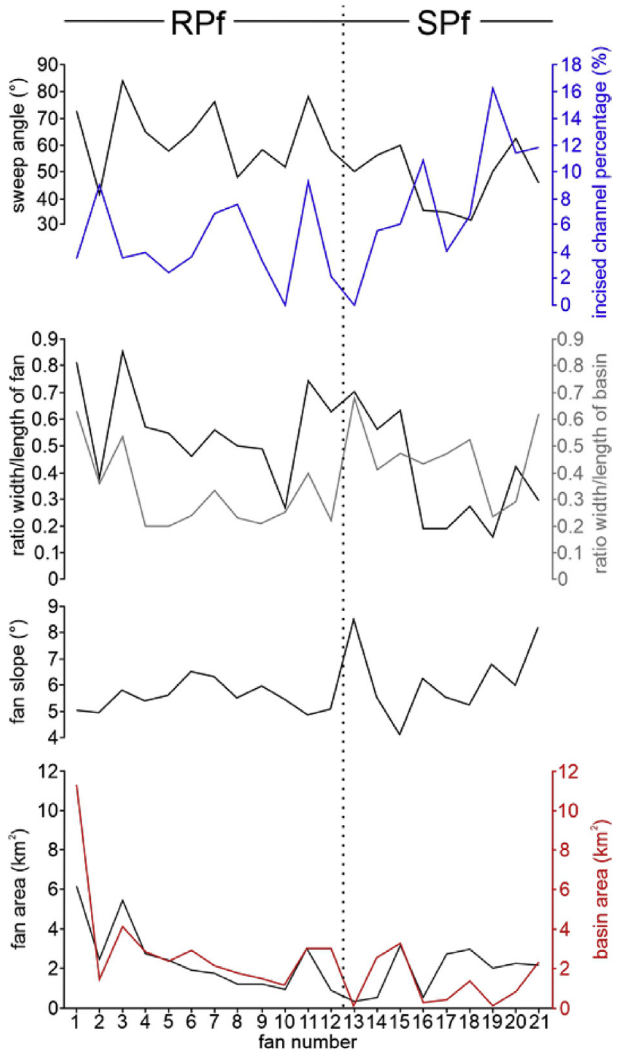

Fig. 6. Graphs showing the distribution of the alluvial fans and drainage basins metrics (listed in Table 1) along the southern Matese mountain front. Locations of alluvial fans and drainage basins are shown in Fig. 5. Black dashed line separates the RPf and the SPf.

basin. These deposits have been interpreted in a former study to be part of a unique alluvial unit referred to as the Ailano lacustrine succession (Ascione et al., 2018). Based on new data in this study, three sedimentary/volcanic units have been distinguished (Fig. 9a).

The lowermost deposits (hereinafter as Ailano Unit 1) consist of thin yellowish silts, which are interlayered with gravel, sand and tufa beds. In the upper part of the succession, a few cm-thick, intensely weathered reddish volcaniclastic layer is found. In the outcrops located in the westernmost part of the study area, deposits of Ailano Unit 1 crop out in the hanging wall of the S-dipping fault that bounds the Mt. Cavuto carbonate ridge on the S, and unconformably rest on Miocene wedge-top basin deposits. Ailano Unit 1 deposits dip 8°–10° towards the N and are displaced by E-W-trending faults.

In the outcrops located in the westernmost part of the study area, deposits of the Ailano Unit 1 are unconformably overlain by thin, dark-grey deposits composed of silts, sands, and fine gravels characterised by fining-upward sequences, which may be related to deposition in an alluvial plain (overbank) or lacustrine environment (Ailano Unit 2, Fig. 9b). The sandy and gravelly fraction contains an abundant amount of volcanic material, primarily consisting of dark-grey, dense juvenile fragments, sub-rounded leucite-bearing lava fragments and a minor amount of chert (sample S-CSP1, Fig. 9b). Deposits of Ailano Unit 2 dip 12°–14° towards the SE and contain a reddish paleosol. The top surface of Ailano Unit 2 deposits has been incised by valleys tens of metres wide oriented roughly E-W (Fig. 9b), which is draped by an at least 30-m-thick pyroclastic succession (Ailano Unit 3). Ailano Unit 3 consists of layers that systematically alternate between whitish, well-sorted pumice beds up to 1 m thick (which are also present in the upper part of the succession) and thicker yellowish to reddish lithified cineritic layers (Fig. 9c). The pumice-rich and cineritic horizons can be ascribed to pyroclastic fall and flow depositional environments, respectively. Several paleosols are interspersed within the Ailano Unit 3 pyroclastic succession. The basal pumice bed (Sample S-CSP2, Fig. 9c) of Ailano Unit 3 has been sampled. Based on geometrical and stratigraphical criteria, one of the cineritic layers of Ailano Unit 3 correlates with a lithologically similar eroded tuff layer ≥2 m thick (Sample S-AIL12, Fig. 9d) and buried below c. 1-m-thick alluvial gravels, which crops out in a man-made trench located in the Volturno River valley. With the aim of obtaining further tephrostratigraphical constraints on Ailano Unit 3, we sampled pyroclastic deposits lithologically comparable to those of the Ailano Unit 3 (i.e., alternating pumice and cineritic layers, Sample PRAT1, Fig. 9e) outcropping in the south-eastern part of the Ciorlano basin, where the units overlie a Middle Pleistocene fluvial terrace (1st order terrace, Ascione et al., 2018).

To the east of the junction between the Lete and Volturno rivers, the succession described above is truncated, with only deposits of Ailano Unit 1 cropping out. A few cm-thick greyish tephra level overlying the eroded surface of the Ailano 1 deposits (Sample S-AIL6, Fig. 8f) has been sampled for tephrostratigraphical/geochronological analyses.

5.3. Tephrostratigraphical data and $^{40}Ar/^{39}Ar$ dating

Most of the sample fraction remaining after pre-treatment consisted of altered juvenile clasts, both limestone and lava lithic fragments, and some leucite-bearing material, with sanidine often found within loose crystals (Table 2). Several other samples taken from the volcaniclastic layers interbedded within the lacustrine sequence underwent the same pre-treatment process but yielded no pristine glass or datable sanidine in the remaining fraction. Since the yields were inconsistent, these samples were not considered for tephrostratigraphical and geochronological analyses.

Overall, only some well-preserved glass fragments were suitable for chemical analysis due to strong alteration of the material, so only a few single-point analyses could be acquired for each sample (Supplementary Table 2). The chemical composition of glasses extracted from the investigated samples falls in the trachyte-phonolite fields of the TAS diagram (Le Maitre, 2005; Supplementary Fig. 2). A general overview of the composition of each sample from this study is provided in Table 3.

In summary, three different clusters of tephras were identified in the investigated area (Supplementary Fig. 2). The youngest layers, S-AIL6 and S-SP2 aged 13.5 ± 4.7 ka and 15.0 ± 1.7 ka, respectively, can be related to the NYT Phlegraean Fields eruption that has a $^{40}Ar/^{39}Ar$ age of 14.9 ± 0.3 ka (Deino et al., 2004). For S-AIL6, no chemical data on glass composition could be obtained and the large error in age (13 ± 4.7 ka) could possibly be due to alteration of sanidine crystals linked to emissions from nearby gas pipes (mapped in Ascione et al., 2018).

Two samples, namely S-AIL15 and S-DR2 aged 37.4 ± 1.2 ka and 42.5 ± 0.7 ka, respectively, are ascribed to the Campanian Ignimbrite eruption, which represents the first caldera-forming explosive event at the Phlegraean Fields. The measured ages of these two

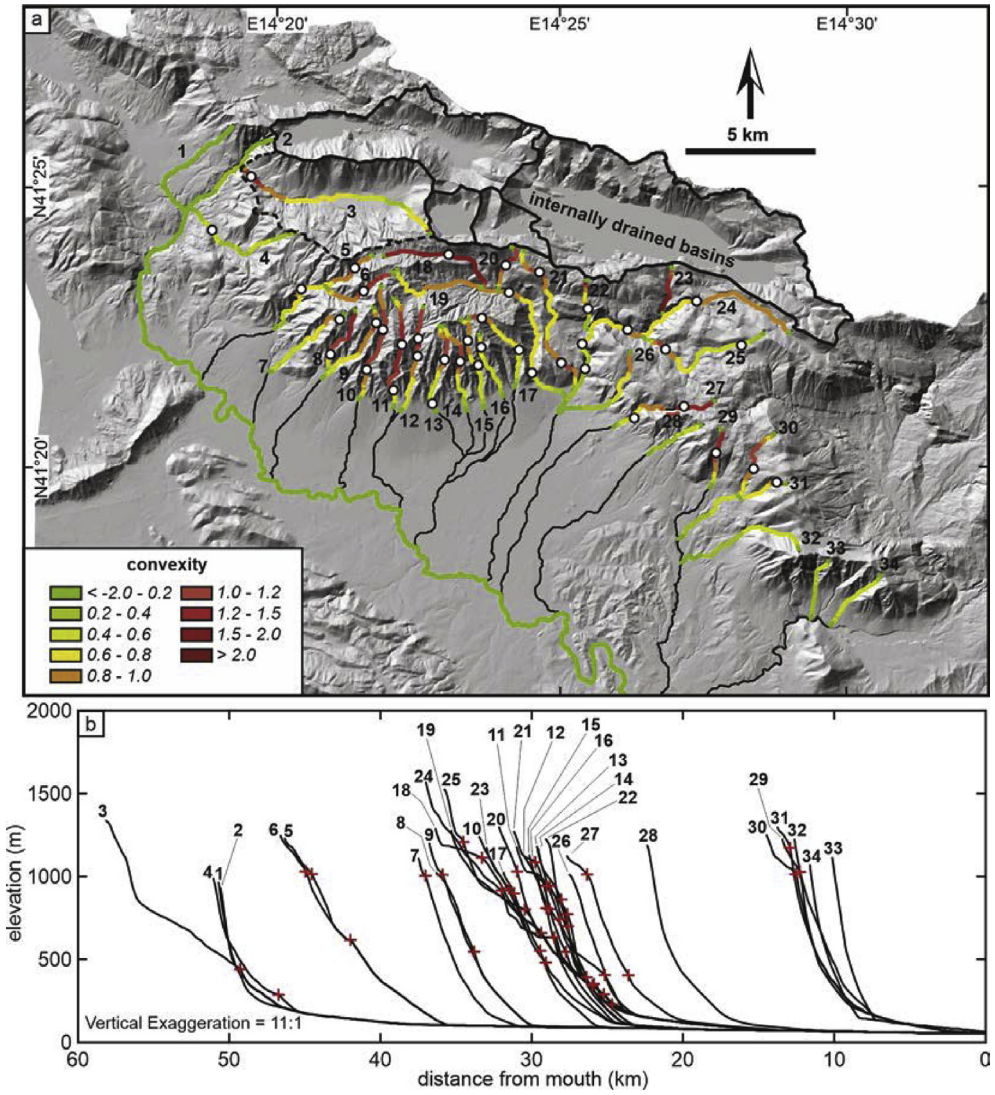

Fig. 7. a) Map of convexity index data for rivers dissecting the southern Matese mountain front. Convexity values obtained using method described in Buscher et al. (2017) and illustrated in inset box. a) Black river lines represent stream reaches not included in convexity analysis but shown in river long profiles of Fig. 7b. White dots indicate knickpoints. b) River long profiles of rivers shown in Fig. 7a. Red crosses indicate knickpoints. Stream profiles and knickpoints shown in Fig. 7a and b created following Whipple et al. (2007) method. Figures modified from Ascione et al. (2018). (For interpretation of the references to colour in this figure legend, the reader is referred to the Web version of this article.)

samples are comparable with the 37.1 to 39.5 ka ages reported by Fedele et al. (2008) for Breccia Museo samples, which represent the proximal counterpart of the Campanian Ignimbrite. Recently, Giaccio et al. (2017) obtained a high-precision $^{40}Ar/^{39}Ar$ age of the Campanian Ignimbrite of 39.85 ± 0.14 ka (95% confidence level), paired with atmospheric radiocarbon ages to provide the first reliable intercalibrated ^{14}C-$^{40}Ar/^{39}Ar$ age of this important tephra marker layer.

The third group of samples are associated with the Roccamonfina HKS leucite-bearing explosive products, which erupted from the volcano in the first stages of activity starting at ca. 600 ka and continuing until ca. 353 ± 5 ka (Brown Leucitic Tuff - Rouchon et al., 2008). Apart from sample S-AIL12 that has been dated at 564.9 ± 2.4 ka (but for which no glass chemical data are available), the chemical composition of glasses extracted from the other samples (S-AIL9, S-SP1, S-CSP2, PRAT1) is quite homogeneous and resembles quite well the composition of Middle Pleistocene tephra layers attributed to Roccamonfina in the distal sequences of Mercure (Giaccio et al., 2014) and Acerno (Petrosino et al., 2014) lacustrine basins. Sample S-CSP1 belongs to this same group and alkali loss, which prevents reliable classification of glasses, and deep analcimization of leucite suggest emplacement has occurred in an underwater environment. The correlation between the single sampled layers with a specific proximal counterpart based only on the mineralogical and chemical data is very speculative, owing to the high repetitiveness of the glass composition in the juvenile products from older Roccamonfina activity and the very low resolution of the proximal data-base.

6. Structural data

A total of 359 meso-scale faults were measured in the Matese ridge area, 161 of which have striations. The cumulative density contour plots of poles to faults show that faults are clustered into three broad sets corresponding to steeply-dipping surfaces striking E-W, NW-SE, and N-S (Fig. 10). Most of the measured faults exhibit normal-sense kinematics (i.e. 95 of the 161) and the contouring of poles to normal faults shows that the sets are the same as the cumulative dataset. The few measured reverse faults strike roughly E-W with N-S oriented, reverse dip-slip displacements.

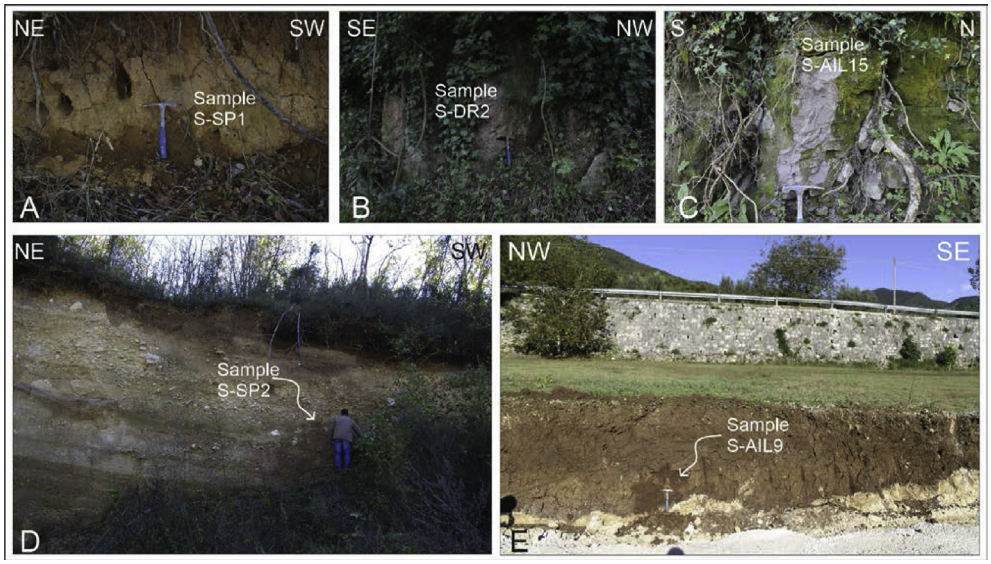

Fig. 8. Tephra layers sampled for tephrostratigraphical analysis and/or $^{40}Ar/^{39}Ar$ dating outcropping along the southern Matese mountain front and shown above for the following samples: A) sample S-SP1; B) sample S-DR2; C) sample S-AIL15; D) sample S-SP2; E) sample S-AIL9. See text for details. Sample locations are reported in Fig. 3.

Strike-slip faults are poorly clustered but both left-lateral and right-lateral faults strike from N-S to NW-SE. For dip-slip faults, and particularly for steeply dipping extensional faults, the clustering of striations is highly affected by small variations in the fault dip or striation rake. In these cases, the rotational axis or rotax (i.e. the slip-normal direction) is much more clustered and better defines the direction of movement (which is perpendicular to the trend of rotaxes; Salvini and Vittori, 1982). In the Matese area, the rotaxes of normal faults are sub-horizontal - thus indicating dip-slip kinematics - and trend N-S, NW-SE, and E-W. In detail, NW-SE-striking normal faults are characterised by NW-SE-trending rotaxes, and the other normal faults that strike N-S and E-W have rotaxes trending E-W and N-S (Fig. 10). These distributions are evidence that the three sets of normal faults, i.e. the NW-SE-, N-S-, and E-W- striking faults, are characterised by almost pure dip-slip kinematics. In the field, normal faults affect the entire exposed unit sequence, from the Quaternary continental and volcanic material (Fig. 11a) down to the Mesozoic carbonates (Fig. 11b). Crosscutting relationships between N-S-, E-W-, and NW-SE-striking extensional faults have been observed and evidence for strike-slip reactivation of normal faults is found in many places including the damage zone of the Fontegreca fault. This fault has a ten-of-meters wide damage zone, where extensional meso-faults occur (Fig. 11c) and strike-slip faults are observed (Fig. 11d) in a narrow (i.e. few meters wide) area of this damage zone, close to the principal displacement zone (*sensu* Tchalenko, 1970). These data highlight that strike-slip movement postdates normal displacement along this major fault. Although extensional movement postdates thrusting and folding, as indicated by regional constraints and by the occurrence of faults in post-orogenic materials (Fig. 11a), many pre-thrusting extensional faults have also been observed. For example, E-W-striking mesoscale syn-sedimentary extensional faults (Fig. 11e) and E-W-striking neptunian dykes (Fig. 11f) have been observed in the Lower Jurassic sequence.

7. Discussion

Quaternary activity of extensional faults at the boundary of the southern Matese mountain front is inferred from high local relief at the transition between the Alife basin and Matese ridge. The new data sets we have collected allow better constraints to be made for the timing and distribution of fault activity during the Quaternary.

The overall geomorphological, morphometrical and stratigraphical data show that features vary with distance along the southern Matese mountain front. Swath profile analysis reveals a variable degree of escarpment maturity along strike. In particular, the change of the mountain front shape from convex in the Raviscanina area, to rectilinear in the Piedimonte Matese area, and to concave in the San Potito Sannitico area (Fig. 2) point to an increase in maturity from NW to SE. The increase in mountain front maturity towards the SE is also inferred from mountain front sinuosity, which is slightly lower in the RPf than in the SPf.

Consistent with the escarpment profiles, features of the drainage network also suggest that the RPf is less mature than other areas of the southern Matese mountain front. Analysis of stream longitudinal profiles indicates that there is a locus of high convexity streams along the RPf, with convexity progressively decreasing away from the centre to the NW and SE. Knickpoints are also mainly clustered in the same area as this locus of high convexity. It is important to note that the convex shape of both the RPF escarpment profiles and long river profiles that dissect the Matese mountain front are not controlled by lithology, as the Triassic dolostones forming the RPf represent the oldest and most erodible units of the Matese ridge carbonate succession.

Geomorphological analysis of the piedmont belt of the southern Matese mountain front has shown that alluvial fan bodies along the RPf are relatively larger with more circular shapes (WLF ~ 0.6) and have low gradients (~5.5°) and high sweep angles (>60°). In contrast, alluvial fan bodies along the SPf are smaller with elongated shapes (WLF ~ 0.4) and have high gradients (>6°) and small sweep angles (<60°). Drainage basin characteristics also differ between the two areas, with relatively large, elongate basins found along the RPf (mean WLD ~ 0.3) and smaller, more circular shaped basins located along the SPf (mean WLD ~ 0.5).

According to Viseras et al. (2003), large fans with high WLF ratios and sweep angles and few incised channels are usually associated with areas affected by high tectonic subsidence, whereas fans with lower WLF ratios and sweep angles that are strongly incised by channels are thought to be less affected by tectonic subsidence. Comparable information can also be inferred from the

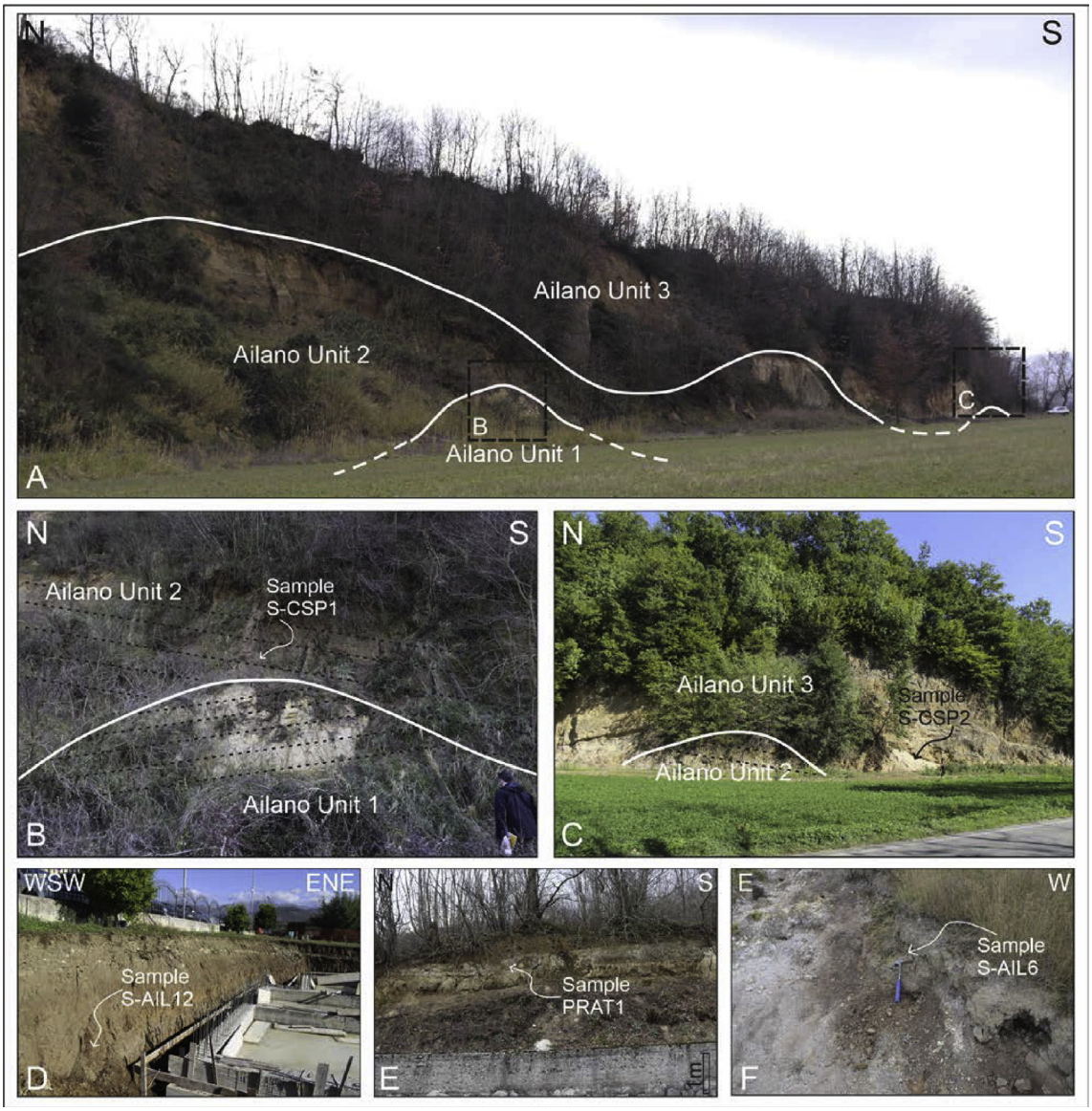

Fig. 9. Alluvial units and tephra layers sampled for tephrostratigraphical analysis and/or $^{40}Ar/^{39}Ar$ dating outcropping west and north of the southern Matese mountain front, i.e. around Ailano and Ciorlano villages, with sample locations shown in Fig. 3. A) Panoramic view of the three sedimentary/volcanic units distinguished in the Ailano area. White lines indicate channel-shaped erosional surfaces (suggesting roughly E-W-trending flow orientations) that separate the three units (dashed where inferred). Black dashed boxes indicate locations of Fig. 9B and C. B) Close-up view of the angular unconformity that separates Ailano Unit 1 from Ailano Unit 2. Dashed black lines indicate bedding. Location of sample S-CSP1 is shown. C) Close-up view of the angular unconformity between Ailano Unit 2 and Ailano Unit 3. Dashed black lines indicate bedding. Location of sample S-CSP2 is shown. D) Location of sample S-AIL12. E) Location of sample PRAT1. F) Location of sample S-AIL6. See text for details.

alluvial fan architecture. For instance, the presence of poorly indented, superimposed alluvial fan bodies along the RPf suggests there has been little to no movement of the deposition locus along the mountain front boundary, implying that fault activity has been continuous (Bull, 2007). Conversely, entrenched alluvial fans along the SPf suggest stream incision is outpacing mountain front uplift, which has led to downstream migration of the active depositional apex (Bull, 2007). Consistent with the geomorphological evidence are the stratigraphical data from the piedmont, which show that deposits of alluvial fan bodies along the RPf are thicker (exceeding 130 m in some areas) than those of alluvial fans along the SPf piedmont (where the late Miocene to Mesozoic bedrock is shallower and crops out locally between the fans), indicating that accommodation space has increased along the RPf relative to the SPf. The geomorphological evidence also reveals differences along the southern Matese mountain front, with the convex upward mountain front, stream long profiles and density of knickpoints along stream profiles indicating that the RPf has experienced a more recent or higher rate of tectonic activity than the SPF. The same is inferred from the shapes of drainage basins sculpted into the mountain front. Elongated drainage basins such as those found along the RPf are usually associated with uplifted footwalls, whereas more circular drainage basins such as those that occur along the SPf are considered to be good indicators of relatively low tectonic uplift (Burbank and Anderson, 2001).

7.1. Morphostratigraphical and chronological constraints of Quaternary fault activity

The relative chronology of geomorphological features and data

Table 2
Sample location, lithological features and ages of the investigated volcaniclastic layers. Sanidine crystals extracted from samples S-SP2, S-SDR2, S-AIL6, S-AIL9, S-AIL12, and S-AIL15 were dated by $^{40}Ar/^{39}Ar$ analysis and produced the ages reported in this table. Sample S-AIL9 had no coherent result and an age plateau could not be calculated.

Sample	Sampling site (UTM-WGS84)		Juvenile fraction	Crystal content	Lithic fragments	$^{40}Ar/^{39}Ar$ dating (ka)
	Northing	Easting				
S-AIL 6	4581810	431313	Rare, badly preserved glass shards	Feldspar crystals with a glass patina		13.5 ± 4.7
S-AIL9	4581420	434971	Very altered leucite- bearing pumice fragments	Abundant feldspar crystals, green clinopyroxene and opaque minerals		undefined
S-AIL12	4581183	430587	Very altered whitish to grey pumice fragments	Abundant feldspar crystals with greyish patina		564.9 ± 2.4
S-AIL15	4586894	431783	Greyish strongly indurated pumice fragments with a dark patina	Abundant feldspar crystals		37.4 ± 1.2
S-SP1	4576465	450996	Altered pumice clasts and ash aggregates	Abundant feldspar, clinopyroxene and leucite crystals		not analysed
S-SP2	4576490	450981	Grey, dense, and altered pumice fragments. Rare obsidian clasts	Feldspar, abundant clinopyroxene, opaque and rare sphene crystals		15.0 ± 1.7
S-DR2	4571690	441887	Well preserved, whitish, vesiculated pumice fragments. Pale honey to brownish platy and blocky glass shards	Abundant feldspar together with several mica crystals, green and brown clinopyroxene grains		42.5 ± 0.7
S-CSP1	45880322	428495	Badly preserved, grey to dark grey, poorly vesicular leucite-bearing juvenile fragments	Abundant loose leucite and feldspar crystals. Rare greenish and brown clinopyroxene grains	Abundant dark leucite, rich in lava, chert and minor limestone fragments.	not analysed
S-CSP2	4580261	428506	Badly preserved, altered pumice fragments with the inner part made up of whitish leucite-bearing pumice fragments with elongated vesicles. Very rare, grey, dense leucite-bearing pumice clasts	Rare feldspar and loose grains of brown clinopyroxene	Abundant limestone and rare leucite- bearing lava lithic fragments	not analysed
PRAT1	4584466	434064	Badly preserved, greyish, leucite-rich pumice fragments	Abundant green and brown clinopyroxene, rare mica and loose feldspar grains	Abundant limestone and leucite- bearing lava lithic fragments	not analysed

on the volcaniclastic layers provide a chronological framework for the evolution of the southern Matese mountain front. $^{40}Ar/^{39}Ar$ dating and tephrostratigraphical analyses have revealed that pyroclastic deposits from the study area were originally emitted from both the Roccamonfina volcano and Phlegraean Fields areas, primarily from the Campanian Ignimbrite and Neapolitan Yellow Tuff eruptions (Section 5.1).

The recovery of HKS pyroclastics from the Roccamonfina volcano, which range in age from c. 600 ka to c. 350 ka (Section 5.1) and overlie and/or are interbedded with alluvial units that surround the southern Matese mountain front, indicate that the Matese ridge has been a topographic high since at least the Middle Pleistocene, prior to c. 350 ka. Tephrostratigraphical correlations point to an age of $\geq$ c. 350 ka for elevated alluvial fan deposits outcropping on top of the RFS (Sections 4.1 and 5.1) and indicate that the age should not be younger than 350 ka for the upper part of the incised 1st generation alluvial fans along the SPf (Sample S-SP1, Section 5.1). The age range of the 1st generation alluvial fan is not significantly constrained by the 15.0 ± 1.7 ka age of the deposit correlated with the NYT (sample S-SP2, Table 2; Section 5.1), which is inset into and therefore postdates the alluvial fan deposits.

The 564.9 ± 2.4 ka $^{40}Ar/^{39}Ar$ age of sample S-AIL12 (Table 2) constrains the age of one of the cineritic layers (from an undefined stratigraphic position) that is part of Ailano Unit 3, overlying Ailano Unit 2 and Ailano Unit 1. Dating of Ailano Unit 3 and correlation of lava fragments contained in the deposits of Ailano Unit 2 with the early products of the Roccamonfina volcano (Section 5.3) suggest an age ~ 600 ka for the Ailano Unit 2 deposits. As for the 1st generation alluvial fans along the SPf, the age range of Ailano Unit 1 is not significantly constrained by the tephra layer with an age of 13.5 ± 4.7 ka (sample S-AIL6 correlated with the NYT, Section 5.1), which unconformably covers the Ailano Unit 1 deposits.

Although lateral/vertical contacts between lacustrine/fluvial and primary pyroclastic deposits (Ailano Unit 1, Ailano Unit 2 and Ailano Unit 3) outcropping to the NW of the RPf and alluvial fans along the RPf are not exposed in the field, geomorphological evidence shows that alluvial fan surfaces in the RPf piedmont are inset into erosional surfaces sculpted into the deposits of Ailano Unit 1 and Ailano Unit 3. Surfaces of the 2nd and 3rd generation alluvial fans along the RPf extend to the Volturno River floodplain, and therefore are coeval with the floodplain. The 2nd and 3rd generation alluvial fans are inset into (and thus postdate) the ignimbrite plateau that stands along the southern margin of the Alife basin. $^{40}Ar/^{39}Ar$ dating of this ignimbrite deposit has provided an age of 42.5 ± 0.7 ka (Sample S-DR2, Table 2) that, together with field evidence and the chemical composition of juvenile clasts, points to a correlation with the Campanian Ignimbrite (Section 5.1). Based on these constraints, an age of <40 ka is established for the deposits of the 2nd and 3rd generation alluvial fans along the RPf. Abundant clastic deposition inferred from the relatively large widths of the 2nd generation alluvial fans may reflect abundant freeze-thaw detrital production associated with the Last Glacial Maximum at c. 20 ka. A Holocene age may be assumed for the 3rd generation alluvial fans along both the RPf and SPf.

7.2. Structural model

Meso-structural data indicate that there are three main sets of extensional faults corresponding to surfaces striking N-S, E-W, and NW-SE, as documented by Calabrò et al. (2003) in this area. Local stretching oriented perpendicular to the main extension direction is a common feature of extensional settings (Ramsay and Huber, 1983), both at the meso-scale (e.g. Gross, 1993; Bai et al., 2002) and at larger scales, where release extensional faults oriented perpendicular to the regional extension direction form in the hanging wall of laterally-terminating extensional faults (e.g. Destro,

Table 3
Composition and possible correlatives of analysed samples.

Sample	Juvenile composition	Possible correlatives	Notes
S-AIL9	High-K phonolitic		Only rare glass fragments were suitable for chemical analysis
S-AIL15	Trachytic		The low FeO content together with the shape of juvenile fragments and altered glass patinas suggest that a secondary mineralization process has taken place
S-SP1	High-K phonolitic		The composition of single fragments is quite variable and most likely due to alteration
S-SP2	Tephriphonolitic, with a minor fraction straddling the boundary between phonolites and trachytes	The chemical composition suggests a correlation with the NYT eruption, which is corroborated by the features typical of NYT juvenile fragments in Apenninic outcrops (pale honey glass shards and blocky shaped dark glass fragments; Amato et al., 2018)	Glass fragments are very well-preserved in shape and hardness
S-DR2	Trachyphonolitic	The chemical composition corresponds well with the composition of glass fragments from the Campanian Ignimbrite eruption (ca. 40 ka – Giaccio et al., 2017). The layer contains both glasses displaying the composition of the main phase of the Campanian Ignimbrite eruption (trachyte with K_2O/Na_2O around 1 – comp. A) and that of the final phases of pyroclastic flows (trachyte with K_2O/Na_2O around 2.5 – comp. B), identified by Tomlinson et al. (2012)	
S-CSP1			Glass extracted from juvenile fragments are very altered and gave no reliable chemical composition due to alkali loss. The leucite crystals included in the juvenile clasts are deeply analcimized
S-CSP2	Phonolitic	The chemical compositiont corresponds well to the Roccamonfina volcano products found in the Mercure Basin by Giaccio et al. (2014) and in the Acerno basin by Petrosino et al. (2014)	Glass fragments are very well-preserved in shape and hardness
PRAT1	Phonolitic	Glass fragments from this layer have a chemical composition that overall resembles the composition of Roccamonfina leucite-bearing distal layers	

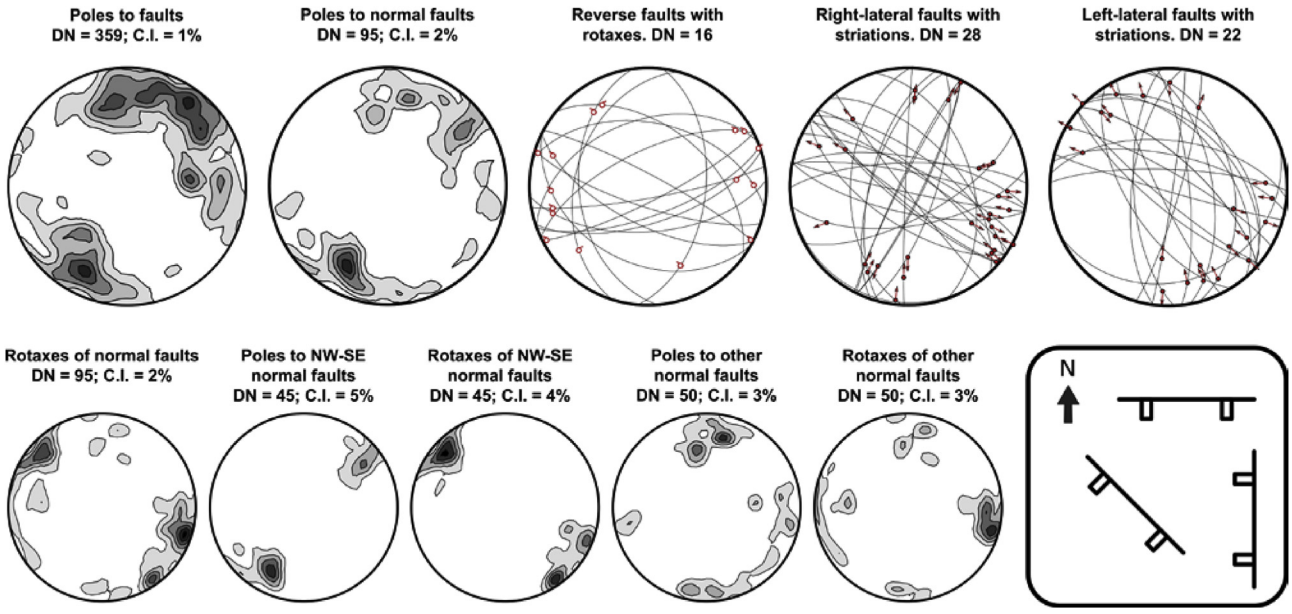

Fig. 10. Stereoplots of faults measured in the Matese massif area (all plots are in stereographic lower hemisphere projection) with scheme showing, in map view, the main sets of extensional faults.

1995; Medwedeff and Krantz, 2002; Tavani et al., 2015). For this reason, the N-S and E-W striking faults are considered to be a single assemblage associated with a single extension direction. No major N-S extensional faults occur in the area, whereas several km-long E-W-striking faults and fault strands are present. Therefore, we interpret the N-S and E-W-striking structures to have formed from N-S extension along E-W-striking faults.

Our geomorphic analysis carried out along major NW-SE- and E-W-striking faults show that both fault systems have been active during the late Quaternary, and thus are roughly coeval. This is supported by observations of meso-structural features pointing to inconsistent cross-cutting relationships between the E-W and N-S

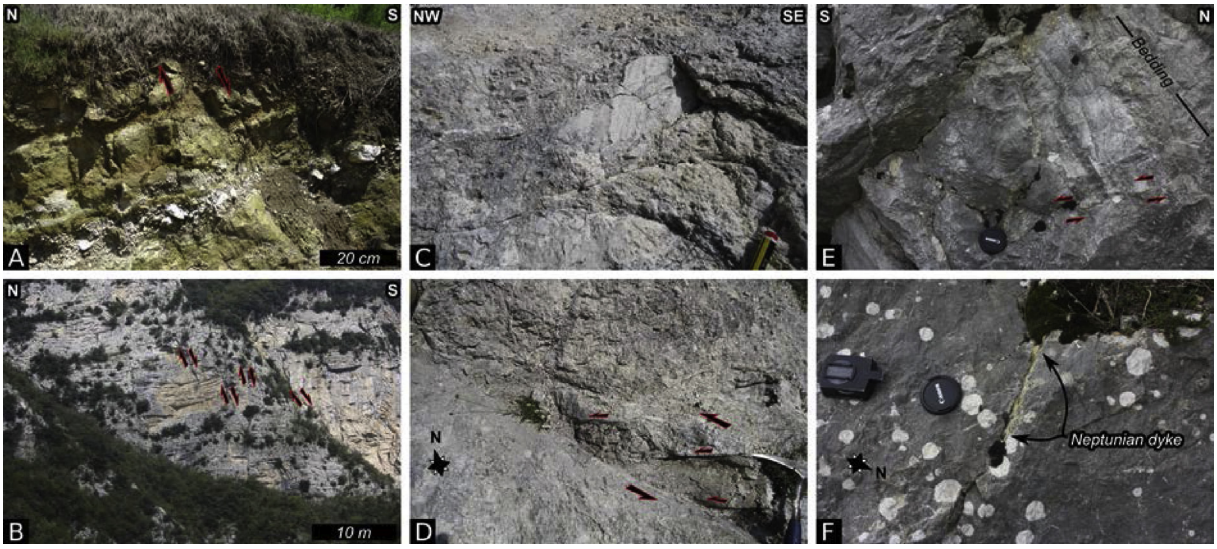

Fig. 11. Examples of meso-structures exposed in the Matese area. A) Meso-scale normal fault affecting the deposits of Ailano Unit 1. B) Jurassic carbonates exposing steeply-dipping normal faults near the town of Piedimonte Matese. C) Close-up frontal view of a cataclastic slip surface with dip-slip striations within the Fontegreca fault damage zone. D) View from top of a left-lateral strike slip fault in the damage zone of the Fontegreca fault, a few meters away from the principal displacement zone. E) Small syn-sedimentary normal fault affecting tilted Jurassic strata. F) E-W-striking neptunian dyke hosted in Lower Jurassic carbonates.

striking faults and the NW-SE striking faults. The occurrence of faults oriented oblique to the dominant extension direction is a common feature of extensional systems and relates to stress heterogeneities that can occur at fault tips (e.g. Pollard and Segall, 1987; Petit and Mattauer, 1995; Homberg et al., 1997), in overstep areas (e.g. Kattenhorn et al., 2000; Agosta et al., 2009), in bends along the fault trace (e.g. Maerten et al., 2002), and within relay zones (e.g. Agosta and Aydin, 2006; Fossen and Rotevatn, 2016). In the Matese area, the N-S extensional features observed at the regional scale can be regarded as local structures framed within the dominant NE-SW-oriented extensional regime, or even with the Quaternary NW-SE-oriented extensional setting documented along the Tyrrhenian margin of the southern Apennines (Caiazzo et al., 2006; Casciello et al., 2006). The fact that the oblique structures are clustered together and define two well-recognisable N-S and E-W striking sets is consistent with the occurrence of inherited Jurassic faults in the study area. As previously illustrated (Fig. 11e, f), E-W-striking Lower Jurassic extensional structures occur in the area. These structures are oriented parallel to the E-W elongated depositional domains created from Early Jurassic rifting (e.g. Calabrò et al., 2003; Iannace et al., 2005), which both point to the occurrence of regionally significant E-W striking faults. During NE-SW extension, the presence of these inherited E-W- striking faults has caused interactions between the fault sets due to the lateral propagation of the newly formed NW-SE-striking faults, forcing bends and, above all, relay ramps to acquire an E-W strike and therefore control local extension in a N-S direction (Fig. 12).

7.3. Morphotectonic scenario

On a regional scale, active NE-SW-trending extension (Cello et al., 1982; Cinque et al., 1993; Hyppolite et al., 1994; Montone et al., 1999; D'Agostino, 2014) is expressed at the surface by active faults with orientations primarily following a ~NW-SE trend (e.g., ITHACA database, http://www.isprambiente.gov.it; Ascione et al., 2007, 2013; Amato et al., 2017). Late Quaternary activity of high-angle normal faults at the southern boundary of the Matese ridge has been suggested by some authors (Cinque et al., 2000; Boncio et al., 2016; Ascione et al., 2018), even if both the style and age of Quaternary fault activity have not been fully appraised to date.

The geomorphological data sets collected from this study indicate that vertical motion along the southern Matese mountain front is unevenly distributed, with the western sector appearing less mature than the SPf. Indeed, the morphometrical data and alluvial fan stratigraphy collectively show that E-W-trending faults at the boundaries of the RPf have experienced either more recent or – as suggested by the outcomes of the structural analysis - higher mean rate displacement than the NW-SE trending faults bounding the SPf. Evidence from the western part of the study area indicates that activity along the E-W-trending faults changed the perimeter of the original alluvial depocenter, which in the early stages included the area around Ailano and, subsequently, became restricted to the area of the Alife basin (Fig. 13). This is inferred from evidence that activity along the E-W trending faults caused multi-stage uplift and incision of alluvial deposits outcropping in the Ailano area (diagrams B and C of Fig. 13). In particular, displacement by E-W-trending faults and incision of Ailano Unit 1 deposits was followed by deposition of Ailano Unit 2 alluvial deposits, which in turn were displaced and eroded by the stream network prior to deposition of the pyroclastic deposits of Ailano Unit 3. During these different stages, deposits of Ailano Unit 1 and Ailano Unit 2 and the underlying Miocene sandstones were uplifted relative to the new adjacent alluvial depocenter (Alife basin), which had limited expansion to the north due to the presence of the E-W-trending faults both in the Ailano area and along the RFS (diagram D of Fig. 13). Based on age of the Ailano Unit 3 and Ailano Unit 2 deposits (section 7.2), activity of faults in the Ailano area may be framed around 600 ka, while activation of the fault at the boundary of the RFS could be younger. South of the RFS lineament, deposits of Ailano Unit 1 and Ailano Unit 2 are buried below a thick sequence of alluvial fan deposits accumulated in the hanging-wall of the E-W-striking normal faults that bound the RPf (Fig. 13). In this area, fault activity created accommodation space that led to deposition of more than 100-m-thick alluvial fan deposits. The Alife basin depocenter was progressively lowered with respect to the piedmont of the SPf as a result of lower mean rate of activity of the NW-SE-striking normal faults at the boundary of the SPf, possibly accompanied by

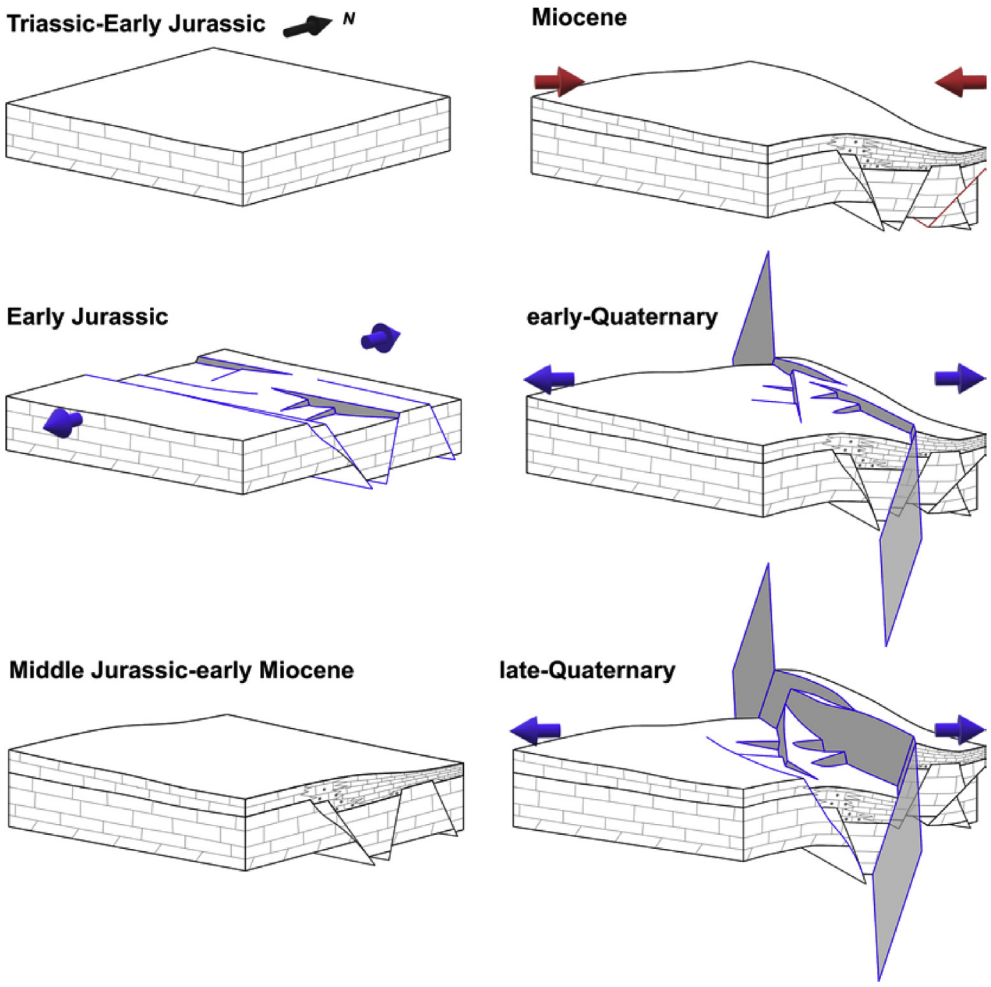

Fig. 12. Scheme showing the tectonic evolution of the study area. Early Jurassic N-S extension led to the development of N-S and E-W striking extensional faults and to the development of E-W elongated host and graben structures, sealed by Middle Jurassic to early Miocene sediments. Miocene NW-SE oriented shortening caused folding, thrusting, and tilting of the Early Jurassic faults. During the Quaternary, NE-SW oriented extension caused the development of NW-SE striking faults. During their growth, these faults linked to, and reactivated, inherited N-S and E-W oriented Jurassic faults, which propagated upward and breached the entire sedimentary sequence.

activation of a N-S trending fault at the eastern basin boundary (sketches D and E of Fig. 13). In response to relative subsidence of the Alife basin with respect to the SPf piedmont, the deposition locus of alluvial fans from the eastern mountain front migrated towards the west, and incised meanders were formed along the Volturno River in the Miocene sandstones that form the Alife basin threshold to the south of the SPf (diagram E of Fig. 13). The occurrence of incised meanders, which dissect the threshold to the east of the Alife basin testifies that alluvial sedimentation episodically balanced basin subsidence. As a result, the >170 m thickness of the alluvial/lacustrine basin fill recovered by the deepest borehole (borehole B4, located to the south of the RFS; Fig. 5), which falls in an area where the carbonate bedrock is shallower (geophysical data in Corniello and Russo, 1990), accounts for only a minimum value of basin subsidence.

As the Alife basin floor is located below the sea level (Supplementary Figure 1), the displacement of the carbonate bedrock along the faults at the boundary of the Matese mountain front exceeds the ~1000 m local relief associated with the RPf. In the areas surrounding Ailano and Ciorlano (location in Fig. 3), intense gas emissions with a crustal signature associated with both the E-W- and N-S-striking extensional fault strands revealed that these faults are associated with large-scale, deep-seated structures (Ascione et al., 2018), such as the several km-long faults that bound the southern Matese ridge mountain front from Raviscanina to Piedimonte Matese.

Because of uncertainties of the subsurface architecture and age of buried alluvial deposits in the Alife basin depocenter, we cannot estimate the rate of fault displacement that has allowed the growth of the RPf. Based on our reconstruction, the early stages of formation of the SMF predate deposition of the Ailano Unit 1, which was limited to the north by the entire SMF, and only later (possibly starting from ~600 ka; Fig. 13) the present-day fault system at the boundary of the RPf was activated. If uncertainties on age (of ~600 ka or dating back to the entire Middle Pleistocene) of the deep part of the buried alluvial fill are considered, the mean displacement rate of faults at the boundary of the RPf has exceeded the ~0.3/0.2 mm/y minimum value of sedimentation rate that we estimate by our data. The inferred long-term displacement rate (>0.2–0.3 mm/y) of the fault system at the boundary of the RPf is consistent with mean values of displacement of faults that, in the southern Apennines, show evidence of activity during the late Quaternary (e.g., Cinque et al., 2000; Papanikolaou and Roberts, 2007; Ascione et al., 2013). Based on our findings, we cannot rule out the possibility that this part of the Matese mountain front may have been the seismogenic source of some poorly known historical

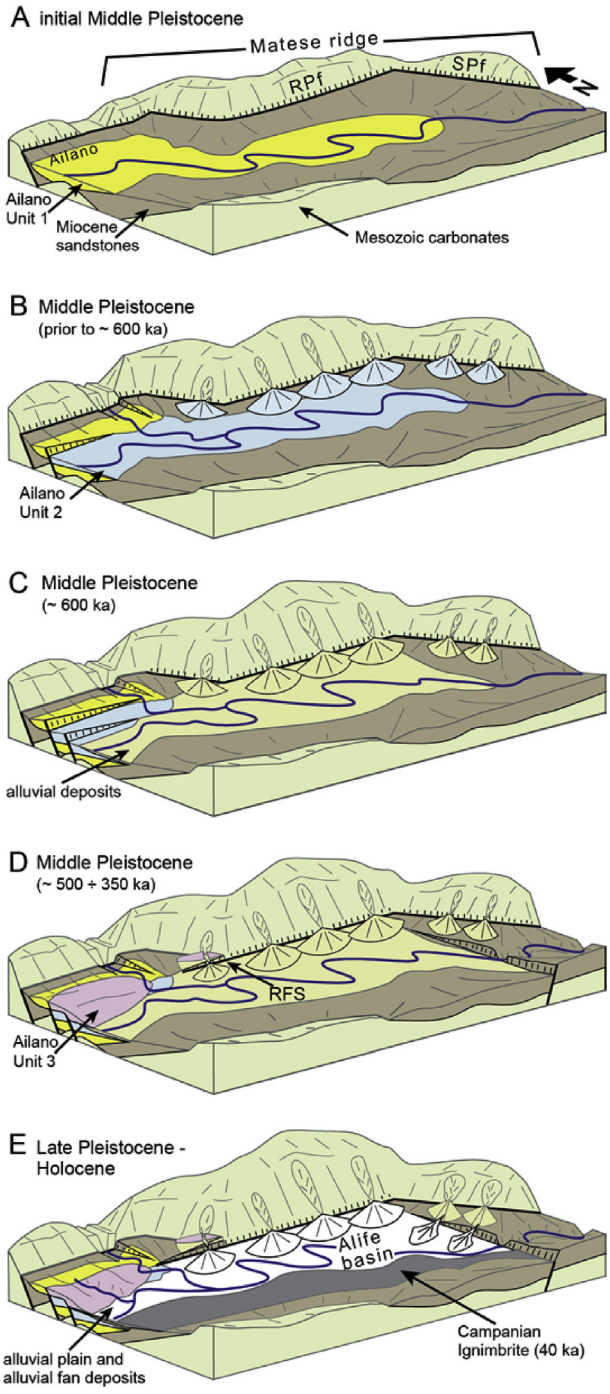

Fig. 13. Main stages (shown in diagrams A to E) of the long-term evolution of the southern Matese mountain front and adjacent alluvial basin. The sketches show the progressive growth of the mountain front and changing spatial distribution of the alluvial depocentres. A: relief of the Matese ridge is subdued; the Ailano Unit 1 is deposited in an alluvial basin located in the hanging wall block of a fault system composed of E-W and NW-SE trending faults; the limit of the alluvial basin is constrained only in the western part of the mapped area. B: deposition, coeval with initial activity of the Roccamonfina volcano, of the Ailano Unit 2 following uplift and tilting of Ailano Unit 1 deposits; early alluvial fan deposition in the piedmont of the uplifting Matese ridge is hypothesised in this stage. C: continuing growth of the Matese mountain front and shifting towards the south of alluvial plain deposition in the Ailano area in response to fault displacement. D: deposition of the volcanic Ailano Unit 3 on top of the eroded surface of the Ailano Unit 2 deposits and alluvial fan in the Raviscanina area; the current perimeter of the mountain front is outlined with formation of the RFS, coeval with de-activation of the western segment of the Matese fault system; growth of the ridge is focused in the SPf. E: continuing growth of the RPf; in the eastern part of the Matese ridge, waning fault activity along the SPf is accompanied by westward shifting of alluvial fan deposition. The thick black line follows perimeter of the active mountain front; black dashes indicate fault scarps.

earthquakes (e.g., the 346 A.D. event, Galadini and Galli, 2004, Fig. 1) and may be the source of moderate to high magnitude earthquakes in the future.

Our study shows how the combination of different data sets may allow unravelling the interaction between tectonic, erosional and sedimentary processes leading to landscape evolution in active mountain belts. Indeed, our case study represents an example of the possible modes of formation and evolution of mountain front-basin systems in extensional setting, which commonly occurs within mountain belts. In such scenarios, the contribution of inherited structures may affect the mountain front-basin system evolution, which may depart from that expected based on theoretical models.

8. Conclusion

To unravel the active tectonic setting of the southern Matese mountain front, we have carried out a wide-ranging investigation of both the mountain front and its piedmont based on the combination of several different data sets. The mutual consistency of the results of all of the morphometric analyses that have been performed provides a robust support to our interpretation of the late Quaternary vertical motions along the southern boundary of the Matese ridge, which is further validated by the analysis of Quaternary rocks and landforms. Crucial constraints to the reconstruction of the late Quaternary tectonic framework of the study area have been provided by the age data and the structural data analysis.

Our investigation of the southern Matese mountain front has shown that in the last ~600 ka, activity along normal faults with prevailing E-W trend has re-shaped the alluvial depocenter to the south of the Matese ridge and identified a locus of tectonic activity with higher mean slip rates located at the boundary of the RPf. The active E-W-striking normal faults in the study area are inherited, reactivated structures which, in the framework of the NE-SW extension active on the regional scale, have interacted with the lateral propagation of the newly formed NW-SE-striking faults causing fault bending and local extension to be oriented N-S. While slow displacement has been recorded along the NW-SE-striking normal faults located at the north-western and south-eastern tips of the southern Matese mountain front, the mean displacement rate of the faults at the boundary of the RPf is in the same order of that of faults, which in the southern Apennines have been active during the late Quaternary.

The Matese ridge is in the seismogenic belt of the southern Apennines. Moderate to high magnitude earthquakes have affected the northern, western and eastern sectors of the Matese ridge in historical times. However, the seismogenic potential of the NW-SE- and E-W-striking extensional fault system that bounds the southern Matese mountain front has not been fully assessed to date (e.g., DISS Working Group, 2018). Despite strong historical seismicity clustering primarily around the study area, our data highlight that it cannot be ruled out that the southern Matese mountain front could be affected by moderate to high magnitude seismicity and that the seismogenic source of some poorly known historical earthquake could be located in this sector of the southern Apennines.

Our case study represents an example of the possible style of formation and development of mountain front-basin systems in extensional setting, and shows how the interaction between tectonic, erosional and sedimentary processes drive the evolution of landscape of active mountain belts.

Author contributions

EV carried out the tectonic geomorphology and morphometry data analysis and wrote the core of the manuscript; JTB performed the morphometry data analysis, contributed part of and edited the manuscript; FJ and SMR performed the geochronological analyses and contributed part of the text; PP performed the tephrostratigraphical analyses and contributed part of the text; ST and AC performed the structural geology data analysis, and ST conceived the structural model and contributed part of the text; AA conceived the study, acquired the funding and wrote part of the manuscript.

Acknowledgements

This study has been partially funded by the Italian Civil Protection Department (DPC, Italy), through the INGV-DPC Seismological Project S1 2014–2015 'Base knowledge improvement for assessing the seismogenic potential of Italy' (responsible of the S1_10 Research Unit: A. Ascione). We wish to acknowledge editor Xiaoping Yang and referees, Lewis Owen and an anonymous referee, for their constructive reviews, which helped us improving our work.

References

Agosta, F., Aydin, A., 2006. Architecture and deformation mechanism of a basin-bounding normal fault in Mesozoic platform carbonates, Central Italy. J. Struct. Geol. 28, 1445–1467.

Agosta, F., Alessandroni, M., Tondi, E., Aydin, A., 2009. Oblique normal faulting along the northern edge of the Majella anticline, central Italy: inferences on structurally controlled hydrocarbon flow. J. Struct. Geol. 31, 674–690.

Amato, V., Aucelli, P.P.C., Cesarano, M., Jicha, B., Lebreton, V., Orain, R., Pappone, G., Petrosino, P., Russo Ermolli, E., 2014. Quaternary evolution of the largest intramontane basin of the Molise Apennine (Southern Italy). Rend Fis Acc Lincei 25 (2). https://doi.org/10.1007/s12210-014-0324-y.

Amato, V., Aucelli, P.P.C., Bellucci Sessa, E., Cesarano, M., Incontri, P., Pappone, G., Valente, E., Vilardo, G., 2017. Multidisciplinary approach for fault detection: integration of PS-InSAR, geomorphological, stratigraphic and structural data in the Venafro intermontane basin (Central-Southern Apennines, Italy). Geomorphology 283, 80–101.

Amato, V., Aucelli, P.P.C., Cesarano, M., Filocamo, F., Leone, N., Petrosino, P., Rosskopf, C.M., Valente, E., Casciello, E., Giralt, S., 2018. Geomorphic response to late Quaternary tectonics in the axial portion of the Southern Apennines (Italy): a case study from the Calore River valley. Earth Surf. Process. Landforms 43, 2463–2480.

Ascione, A., Caiazzo, C., Cinque, A., 2007. Recent faulting in southern Apennines (Italy): geomorphic evidence, spatial distribution and implications for rates of activity. Ital. J. Geosci. 126 (2), 293–305.

Ascione, A., Ciarcia, S., Di Donato, V., Mazzoli, S., Vitale, S., 2012. The Pliocene-Quaternary wedge-top basins of southern Italy: an expression of propagating lateral slab tear beneath the Apennines. Basin Res. 24 (4), 456–474.

Ascione, A., Mazzoli, S., Petrosino, P., Valente, E., 2013. A decoupled kinematic model for active normal faults: insights from the 1980, MS = 6.9 Irpinia earthquake, southern Italy. Geol. Soc. Am. Bull 125 (7–8), 1239–1259.

Ascione, A., Ciotoli, G., Bigi, S., Buscher, J., Mazzoli, S., Ruggiero, L., Sciarra, A., Tartarello, M.C., Valente, E., 2018. Assessing mantle versus crustal sources for non-volcanic degassing along fault zones in the actively extending southern Apennines mountain belt (Italy). Geol. Soc. Am. Bull. 130 (9–10), 1697–1722. https://doi.org/10.1130/B31869.1.

Aucelli, P.P.C., Cesarano, M., Di Paola, G., Filocamo, F., Rosskopf, C.M., 2013. Geomorphological map of the central sector of the Matese Mountains (Southern Italy): an example of complex landscape evolution in a Mediterranean mountain environment. J. Maps 9 (4), 604–616. https://doi.org/10.1080/17445647.2013.840054.

Attal, M., Cowie, P.A., Whittaker, A.C., Hobley, D., Tucker, G.E., Roberts, G.P., 2011. Testing fluvial erosion models using the transient response of bedrock rivers to tectonic forcing in the Apennines, Italy. J. Geophys. Res. 116, F02005. https://doi.org/10.1029/2010JF001875.

Bai, T., Maerten, L., Gross, M.R., Aydin, A., 2002. Orthogonal cross joints: do they imply a regional stress rotation? J. Struct. Geol. 24, 77–88.

Boncio, P., Dichiarante, A.M., Auciello, E., Saroli, M., Stoppa, F., 2016. Normal faulting along the western side of the matese mountains: implications for active tectonics in the central Apennines (Italy). J. Struct. Geol. 82, 16–36.

Boschi, E., Guidoboni, E., Ferrari, G., Valensise, G., Gasperini, P., 1997. Catalogue of Strong Italian Earthquakes, 461 B.C. To 1990. ING-SGA, Bologna, Italy.

Bull, W.B., 2007. Tectonic Geomorphology of Mountains: a New Approach to Paleoseismology. John Wiley & Sons, Chichester.

Bull, W.B., McFadden, L.D., 1977. Tectonic geomorphology north and south of the Garlock fault, California. In: Doehring, D.O. (Ed.), Geomorphology in Arid Regions. Proceedings of the Eighth Annual Geomorphology Symposium. State University of New York, Binghamton, pp. 115–138.

Burbank, D.W., Anderson, R.S., 2001. Tectonic Geomorphology. John Wiley & Sons, Chichester.

Butler, R.W.H., Corrado, S., Mazzoli, S., Donatis, M.D., Di Bucci, D., Naso, G., Scrocca, D., Nicolai, C., Zucconi, V., 2000. Time and space variability of «thin-skinned» and «thick-skinned» thrust tectonics in the Apennines (Italy). Rend. Lincei-Sci. Fis. 11, 5–39. https://doi.org/10.1007/BF02904594.

Butler, R.W.H., Mazzoli, S., Corrado, S., De Donatis, M., Di Bucci, D., Gambini, R., Naso, G., Nicolai, C., Scrocca, D., Shiner, P., Zucconi, V., 2004. Applying thick-skinned tectonic models to the Apennine thrust belt of Italy: limitations and implications. In: McClay, K.R. (Ed.), Thrust Tectonics and Petroleum Systems, vol. 82. A.A.P.G. Memoir., pp. 647–667

Buscher, J.T., Ascione, A., Valente, E., 2017. Decoding the role of tectonics, incision and lithology on drainage divide migration in the Mt. Alpi region, southern Apennines, Italy. Geomorphology 276, 37–50.

Caiazzo, C., Ascione, A., Cinque, A., 2006. Late Tertiary-Quaternary tectonics of the southern Apennines (Italy): new evidences from the Tyrrhenian slope. Tectonophysics 421, 23–51.

Calabrò, R.A., Corrado, S., Di Bucci, D., Robustini, P., Tornaghi, M., 2003. Thin-skinned vs. thick-skinned tectonics in the matese massif, central–southern Apennines (Italy). Tectonophysics 377, 269–297. https://doi.org/10.1016/j.tecto.2003.09.010.

Casciello, E., Cesarano, M., Pappone, G., 2006. Extensional detachment faulting on the Tyrrhenian margin of the southern Apennines contractional belt (Italy). J. Geol. Soc. Lond. 163, 617–629.

Cello, G., Guerra, I., Tortorici, L., Turco, E., Scarpa, R., 1982. Geometry of the neotectonic stress field in southern Italy: geological and seismological evidence. J. Struct. Geol. 4, 385–393.

Cello, G., Tondi, E., Micarelli, L., Mattioni, L., 2003. Active tectonics and earthquake sources in the epicentral area of the 1857 Basilicata earthquake (Southern Italy). J. Geodyn. 36, 37–50.

Cinque, A., Patacca, E., Scandone, P., Tozzi, M., 1993. Quaternary kinematic evolution of the Southern Apennines. Relationships between surface geological features and deep lithospheric structures. Ann. Geophys. 36, 249–260.

Cinque, A., Ascione, A., Caiazzo, C., 2000. Distribuzione spazio temporale e caratterizzazione della fagliazione quaternaria in Appennino Meridionale. In: Galadini, F., Meletti, C., Rebez, A. (Eds.), Le Ricerche del GNDT nel campo della pericolosità sismica, pp. 203–218.

Corniello, A., Russo, D., 1990. La piana del medio corso del F. Volturno (Campania) idrogeologia e vulnerabilità all'inquuinamento delle falde. In: Atti I Convegno Nazionale sulla Protezione e Gestione delle Acque Sotterranee, pp. 131–148.

Deino, A.L., Orsi, G., De Vita, S., Piochi, M., 2004. The age of the Neapolitan Yellow Tu¡ caldera-forming eruption (Campi Flegrei caldera ^ Italy) assessed by $^{40}Ar/^{39}Ar$ dating method. J. Volcanol. Geotherm. Res. 133, 157–170.

Destro, N., 1995. Release fault: a variety of cross fault in linked extensional fault systems, in the Sergipe-Alagoas Basin, NE Brazil. J. Struct. Geol. 17, 615–629.

D'Agostino, N., 2014. Complete seismic release of tectonic strain and earthquake recurrence in the Apennines (Italy). Geophys. Res. Lett. 41, 1155–1162. https://doi.org/10.1002/2014GL059230.

D'Amico, S., Cammarata, L., Cangemi, M., Cavallaro, D., Di Martino, R.M., Firetto Carlino, M., 2014. Seismic moment tensors and regional stress in the area of the December 2013– January 2014, Matese earthquake sequence (Italy). J. Geodyn. 82, 118–124.

de Polo, C.M., Anderson, J.G., 2000. Estimating the slip rates of normal faults in the Great Basin, USA. Basin Res. 12, 227–240.

Di Bucci, D., Massa, B., Tornaghi, M., Zuppetta, A., 2005. Structural setting of the 1688 Sannio earthquake epicentral area (Southern Italy) from surface and subsurface data. J. Geodyn. 40 (2), 294–315. https://doi.org/10.1016/j.jog.2005.07.008.

DISS Working Group, 2018. Database of Individual Seismogenic Sources (DISS), Version 3.2.1: A Compilation of Potential Sources for Earthquakes Larger than M 5.5 in Italy and Surrounding Areas. https://doi.org/10.6092/INGV.IT-DISS3.2.1. http://diss.rm.ingv.it/diss. (Accessed 28 January 2019).

Ellis, M.A., Densmore, A.L., Anderson, R.S., 1999. Development of mountainous topography in the Basin region, USA. Basin Res. 11, 21–41.

England, P., Molnar, P., 1990. Surface uplift, uplift of rocks, and exhumation of rocks. Geology 18, 1173–1177.

Esposito, E., Luongo, G., Marturano, A., Porfido, S., 1987. Il terremoto di S. Anna del 26 Luglio 1805. Mem. Soc. Geol. It. 37, 171–191.

Fedele, L., Scarpati, C., Lanphere, M., Melluso, L., Morra, V., Perrotta, A., Ricci, G., 2008. The Breccia Museo formation, Campi Flegrei, southern Italy: geochronology, chemostratigraphy and relationship with the Campanian Ignimbrite eruption. Bull. Volcanol. 70 (10), 1189–1219.

Ferranti, L., Milano, G., Burrato, P., Palano, M., Cannavò, F., 2015. The seismogenic structure of the 2013–2014 Matese seismic sequence, Southern Italy:

implication for the geometry of the Apennines active extensional belt. Geophys. J. Int. 201, 823–837.
Ferrarini, F., Boncio, P., de Nardis, R., Pappone, G., Cesarano, M., Aucelli, P.P.C., Lavecchia, G., 2017. Segmentation pattern and structural complexities in seismogenic extensional settings: the North Matese Fault System (Central Italy). J. Struct. Geol. 95, 93–112.
Fossen, H., Rotevatn, A., 2016. Fault linkage and relay structures in extensional settings – a review. Earth Sci. Rev. 154, 14–28.
Fracassi, U., Valensise, G., 2007. Unveiling the sources of the catastrophic 1456 multiple earthquake: hints to anunexplored tectonic mechanism in southern Italy. Bull. Seismol. Soc. Am. 97 (3), 725–748.
Frankel, K.L., Pazzaglia, F.J., 2006. Mountain fronts, base-level fall, and landscape evolution: insights from the southern Rocky Mountains. In: Willett, S.D., Hovius, N., Brandon, M.T., Fisher, D.M. (Eds.), Tectonics, Climate, and Landscape Evolution. Geological Society of America Special Paper 398, Penrose Conference Series, pp. 419–434. https://doi.org/10.1130/2006.2398(26.
Galadini, F., Galli, P., 2004. The 346 A.D. earthquake (central-southern Italy): an archaeoseismological approach. Ann Geophys. Italy 47 (2–3), 885–905.
Galli, P., Galadini, F., 2003. Disruptive earthquakes revealed by faulted archaeological relics in Samniun (Molise, southern Italy). Geophys. Res. Lett. 30 (5), 1266.
Galli, P., Naso, G.A., 2009. Unmasking the 1349 earthquake source (southern Italy): paleoseismological andarchaeoseismological indications from the Aquae Iuliae fault. J. Struct. Geol. 31, 128–149.
Galli, P., Giaccio, B., Messina, P., Peronace, E., Amato, V., Naso, G., Nomade, S., Pereira, A., Piscitelli, S., Bellanova, J., Billi, A., Blamart, D., Galderisi, A., Giocoli, A., Stabile, T., Thil, F., 2017. Middle to Late Pleistocene activity of the northern Matese fault system (southern Apennines, Italy). Tectonophysics 699, 61–81.
Gasperini, P., Bernardini, F., Valensise, G., Boschi, E., 1999. Defining seismogenic sources from historical earthquake felt reports. Bull. Seismol. Soc. Am. 89, 94–110.
Giaccio, B., Galli, P., Peronace, E., Arienzo, I., Nomade, S., Cavinato, G.P., Mancini, M., Messina, P., Sottili, G., 2014. A 560–440 ka tephra record from the Mercure Basin, southern Italy: volcanological and tephrostratigraphic implications. J. Quat. Sci. 29 (3), 232–248.
Giaccio, B., Hajdas, I., Isaia, R., Deino, A., Nomade, S., 2017. High-precision 14C and 40Ar/39Ar dating of the Campanian Ignimbrite (Y-5) reconciles the time-scales of climatic-cultural processes at 40 ka. Sci. Rep-UK 7, 45940. https://doi.org/10.1038/srep45940.
Gross, M.R., 1993. The origin and spacing of cross joints: examples from the Monterey Formation, Santa Barbara Coastline, California. J. Struct. Geol. 15, 737–751.
Hack, J.T., 1957. Studies of longitudinal streamprofiles in Virginia and Maryland. U. S. Geol. Surv. Prof. Pap. 249-B, 45–97.
Harkins, N.W., Anastasio, D.J., Pazzaglia, F.J., 2005. Tectonic geomorphology of the Red Rock fault, insights into segmentation and landscape evolution of a developing range front normal fault. J. Struct. Geol. 27, 1925–1939.
Homberg, C., Hu, J.C., Angelier, J., Bergerat, F., Lacombe, O., 1997. Characterization of stress perturbations near major fault zones: insights from 2D distinct-element numerical modelling and field studies (Jura mountains). J. Struct. Geol. 19, 703–718.
Hovius, N., 1996. Regular spacing of drainage outlets from linear mountain belts. Basin Res. 8 (1), 29–44.
Hyppolite, J.C., Angelier, J., Roure, F., Casero, P., 1994. A major geodynamic change revealed by Quaternary stress patterns in the Southern Apennines (Italy). Tectonophysics 230, 199–210.
Iannace, A., Parente, M., Zamparelli, V., 2005. An early Jurassic submarine scarp in the western Matese mountains. Ital. J. Geosci. 124, 215–221.
Kattenhorn, S.A., Aydin, A., Pollard, D.D., 2000. Joints at high angles to normal fault strike: an explanation using 3D numerical models of fault perturbed stress fields. J. Struct. Geol. 22, 1–23.
Keller, E.A., Pinter, N., 2002. Active Tectonics – Earthquakes, Uplift, and Landscape, second ed. Prentice Hall, London.
Kirby, E., Whipple, K., 2001. Quantifying differential rock-uplift rates via stream profile analysis. Geology 29, 415–418.
Koppers, A.A.P., 2002. ArArCalc – software for $^{40}Ar/^{39}Ar$ age calculation. Comput. Geosci. 28 (5), 605–619.
Lee, J.Y., Marti, K., Severinghaus, J.P., Kawamura, K., Yoo, H.S., Lee, J.B., Kim, J.S., 2006. A redetermination of the isotopic abundances of atmospheric Ar. Geochim. Cosmochim. Acta 70 (17), 4507–4512. Comput. Geosci. 28 (5), 605-619.
Le Maitre, R.W., 2005. Igneous rocks. In: A Classification and Glossary of Terms. Recommendations of the Internal Union of Geological Sciences Subcommission on the Systematics of Igneous Rocks. Cambridge University Press, Cambridge.
Locati, M., Camassi, R., Stucchi, M., 2011. DBMI11, the 2011 Version of the Italian Macroseismic Database. http://emidius.mi.ingv.it/DBMI11. (Accessed 28 January 2019).
Luiso, P., Paoletti, V., Nappi, R., La Manna, M., Cella, F., Gaudiosi, G., Fedi, M., Iorio, M., 2018. A multidisciplinary approach to characterize the geometry of active faults: the example of Mt. Massico, Southern Italy. Geophys. J. Int. 213 (3), 1673–1681. https://doi.org/10.1093/gji/ggy080.
Maerten, L., Gillespie, P., Pollard, D.D., 2002. Effects of local stress perturbation on secondary fault development. J. Struct. Geol. 24, 145–153.
Mahmood, S.A., Gloaguen, R., 2012. Appraisal of active tectonics in Hindu Kush: insights from DEM derived geomorphic indices and drainage analysis. Geosci. Front. 3 (4), 407–428.
Mazzoli, S., D'Errico, M., Aldega, L., Corrado, S., Invernizzi, C., Shiner, P., Zattin, M., 2008. Tectonic burial and "young" (<10 Ma) exhumation in the southern Apennines fold-and-thrust belt. Geology 36 (3), 243–246.
Mazzoli, S., Ascione, A., Buscher, J.T., Pignalosa, A., Valente, E., Zattin, M., 2014. Low-angle normal faulting and focused exhumation associated with late Pliocene change in tectonic style in the Southern Apennines. Tectonics 33, 1802–1818.
Medwedeff, D.A., Krantz, R.W., 2002. Kinematic and analog modeling of 3-D extensional ramps: observations and a new 3-D deformation model. J. Struct. Geol. 24 (4), 763–772.
Miccadei, E., Paron, P., Piacentini, T., 2004. The SW escarpment of Montagna del Morrone (Abruzzi, central Italy): geomorphology of a fault-generated mountain front. Geogr. Fis. Din. Quaternaria 27, 55–87.
Michetti, A.M., Ferreli, L., Esposito, E., Porfido, S., Blumetti, A.M., Vittori, E., Serva, L., Roberts, G.P., 2000. Ground effects during the 9 September 1998, Mw = 5.6 Lauria earthquake and the seismic potential of the "Aseismic" Pollino region in southern Italy. Seismol Res. Lett. 71 (1), 31–46. https://doi.org/10.1785/gssrl.71.1.31.
Montone, P., Amato, A., Pondrelli, S., 1999. Active stress map of Italy. J. Geophys. Res. 104 (B11), 25595–25610.
Papanikolaou, I.D., Roberts, G.P., 2007. Geometry, kinematics and deformation rates along the active normal fault system in the southern Apennines: implications for fault growth. J. Struct. Geol. 29 (1), 166–188.
Patacca, E., Scandone, P., 2001. Late thrust propagation and sedimentary response in the thrust- belt-foredeep system of the Southern Apennines (Pliocene-Pleistocene). In: Vai, G.B., Martini, I.P. (Eds.), Anatomy of an Orogen: the Apennines and Adjacent Mediterranean Basins. Kluwer Academic Publishers, London, pp. 401–440.
Pérez-Peña, J.V., Al-Awabdeh, M., Azañón, J.M., Galve, J.P., Booth-Rea, G., Notti, D., 2017. SwathProfiler and NProfiler: two new ArcGIS Add-ins for the automatic extraction of swath and normalized river profiles. Comput. Geosci. 104, 135–150.
Petit, J.-P., Mattauer, M., 1995. Palaeostress superimposition deduced from mesoscale structures in limestone: the Matelles exposure, Languedoc, France. J. Struct. Geol. 17, 245–256.
Petrosino, P., Jicha, B.J., Mazzeo, F.C., Russo Ermolli, E., 2014. A high-resolution tephrochronological record of MIS 14-12 in the southern Apennines (Acerno basin, Italy). J. Volcanol. Geotherm. Res. 274, 34–50.
Petrosino, P., Jicha, B.J., Mazzeo, F.C., Ciaranfi, N., Girone, A., Maiorano, P., Marino, M., 2015. The Montalbano Jonico marine succession: an archive for distal tephra layers at the Early-Middle Pleistocene boundary in southern Italy. Quat. Int. 383, 89–103.
Pollard, D.D., Segall, P., 1987. Theoretical displacements and stresses near fractures in rock: with application to faults, joints, veins, dikes, and solution surfaces. In: Atkinson, B.K. (Ed.), Fracture Mechanics of Rock. Academic Press, London, pp. 277–349.
Porfido, S., Esposito, E., Vittori, E., Tranfaglia, G., Guerrieri, L., Pece, R., 2007. Seismically induced ground effects of the 1805, 1930 and 1980 earthquakes in the Southern Apennines (Italy). It. J. Geosci. 126 (2), 333–346.
Ramsay, J.G., Huber, M.I., 1983. The Techniques of Modern Structural Geology, vol. 1. Academic Press, London. Strain Analysis.
Regalla, C.A., Anastasio, D.J., Pazzaglia, F.J., 2007. Characterization of the Monument hill Fault System and implications for the active tectonics of the red rock valley, southwestern Montana. J. Struct. Geol. 29 (8), 1339–1352.
Renne, P.R., Balco, G., Ludwig, K.R., Mundil, R., Minb, K., 2011 (2010). Geochim. Cosmochim. Ac. In: Renne, P.R., et al. (Eds.), Response to the comment by W.H. Schwarz et al. on " Joint Determination of 40K Decay Constants and 40Ar */40K for the Fish Canyon Sanidine Standard, and Improved Accuracy for 40Ar/39Ar Geochronology", vol. 75, pp. 5097–5100 (17).
Renne, P.R., Deino, A.L., Hilgen, F.J., Kuiper, F.K., Mark, D.F., Mitchell III, W.S., Morgan, L.E., Mundil, R., Smith, J., 2013. Time scales of critical events around the Creataceous – Paleogene boundary. Science 339 (6120), 684–687.
Rouchon, V., Gillot, P.Y., Quidelleur, X., Chiesa, S., Floris, B., 2008. Temporal evolution of the Roccamonfina volcanic complex (Pleistocene), central Italy. J. Volcanol. Geotherm. Res. 177 (2), 500–514.
Rovida, A., Locati, M., Camassi, R., Lolli, B., Gasperini, P., 2016. CPTI15, the 2015 Version of the Parametric Catalogue of Italian Earthquakes. Istituto Nazionale di Geofisica e Vulcanologia. http://doi.org/10.6092/INGV.IT-CPTI15. (Accessed 28 January 2019).
Salvini, F., Vittori, E., 1982. Analisi strutturale della linea Olevano-Antrodoco-Posta (Ancona-Anzio Auct.): metodologia di studio delle deformazioni fragili e presentazione del tratto meridionale. Mem. Soc. Geol. It. 24, 337–355.
Sartori, R., 1990. The main results of ODP Leg 107 in the frame of Neogene to Recent geology of PeriTyrrhenian areas. In: Kastens, K.A., Mascle, J., et al. (Eds.), Proceedings of the Ocean Drilling Program, Scientific Results, vol. 107. Ocean Drilling Program, College Station, TX, pp. 715–730.
Savelli, C., Schreider, A.A., 1991. The opening processes in the deep Tyrrhenian basins of Marsili and Vavilov, as deduced from magnetic and chronological evidence of their igneous crust. Tectonophysics 190, 119–131.
Serva, L., Esposito, E., Guerrieri, L., Porfido, S., Vittori, E., Comerci, V., 2007. Environmental effects from five historical earthquakes in southern Apennines (Italy) and macroseismic intensity assessment: contribution to INQUA EEE Scale Project. Quat. Int. 173–174, 30–44. https://doi.org/10.1016/j.quaint.2007.03.015.
Shiner, P., Beccacini, A., Mazzoli, S., 2004. Thin-skinned versus thick-skinned structural models for Apulian carbonate reservoirs: constraints from the Val d'Agri fields, S Apennines, Italy. Mar. Pet. Geol. 21, 805–827.
Tavani, S., Storti, F., Lacombe, O., Corradetti, A., Muñoz, J.A., Mazzoli, S., 2015.

A review of deformation pattern templates in foreland basin systems and fold-and-thrust belts: implications for the state of stress in the frontal regions of thrust wedges. Earth Sci. Rev. 141, 82–104.
Tchalenko, J.S., 1970. Similarity between shear zones of different magnitudes. Geol. Soc. Am. Bull. 81 (6), 1625–1640.
Tomlinson, E.L., Arienzo, I., Civetta, L., Wulf, S., Smith, V.C., Hardiman, M., Lane, C.S., Carandente, A., Orsi, G., Rosi, M., Muller, W., Menzies, M.A., 2012. Geochemistry of the Phlegraean Fields (Italy) proximal sources for major Mediterranean tephras: implications for the dispersal of Plinian and co-ignimbritic components of explosive eruptions. Geochem. Cosmochim. Acta 93, 102–128.
Valente, E., Ascione, A., Ciotoli, G., Cozzolino, M., Porfido, S., Sciarra, A., 2018. Do moderate magnitude earthquakes generate seismically induced ground effects? The case study of the Mw = 5.16, 29th December 2013 Matese earthquake (southern Apennines, Italy). Int. J. Earth Sci. 107, 517–537. https://doi.org/10.1007/s00531-017-1506-5.
Viseras, C., Calvache, M.L., Soria, J.M., Fernández, J., 2003. Differential features of alluvial fans controlled by tectonic or eustatic accommodation space. Examples from the Betic Cordillera, Spain. Geomorphology 50 (1), 181–202.
Vitale, S., Ciarcia, S., 2013. Tectono-stratigraphic and kinematic evolution of the southern Apennines/Calabria-Peloritani Terrane system (Italy). Tectonophysics 583, 164–182.
Vitale, S., Ciarcia, S., 2018. Tectono-stratigraphic setting of the Campania region (southern Italy). J. Maps 14 (2), 9–21.
Wallace, R.E., 1977. Profiles and ages of young fault scarps, north-central Nevada. Geol. Soc. Am. Bull. 88, 1267–1281.
Whipple, K., Wobus, C., Crosby, B., Kirby, E., Sheehan, D., 2007. New tools for quantitative geomorphology: extraction and interpretation of stream profiles from digital topographic data. In: Short Course Presented at Geological Society of America Annual Meeting, Denver, CO. Available at: http://www.geomorphtools.org.
Whittaker, A.C., 2012. How do landscapes record tectonics and climate? Lithosphere 4, 160–164. https://doi.org/10.1130/RF.L003.1.
Whittaker, A.C., Cowie, P.A., Attal, M., Tucker, G.E., Roberts, G.P., 2007. Bedrock channel adjustment to tectonic forcing: implications for predicting river incision rates. Geology 35, 103–106. https://doi.org/10.1130/G23106A.1.
Whittaker, A.C., Attal, M., Cowie, P.A., Tucker, G.E., Roberts, G., 2008. Decoding temporal and spatial patterns of fault uplift using transient river long profiles. Geomorphology 100 (3–4), 506–526.
Young, A., 1972. Slopes. Oliver and Boyd, Edinburgh.